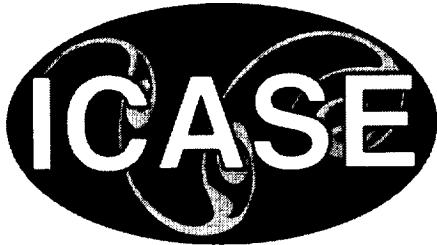


NASA/CR-2002-211947
ICASE Report No. 2002-38



Analysis of Composite Skin-stiffener Debond Specimens using Volume Elements and a Shell/3D Modeling Technique

Ronald Krueger
ICASE, Hampton, Virginia

Pierre J. Minguet
The Boeing Company, Philadelphia, Pennsylvania



October 2002

The NASA STI Program Office . . . in Profile

Since its founding, NASA has been dedicated to the advancement of aeronautics and space science. The NASA Scientific and Technical Information (STI) Program Office plays a key part in helping NASA maintain this important role.

The NASA STI Program Office is operated by Langley Research Center, the lead center for NASA's scientific and technical information. The NASA STI Program Office provides access to the NASA STI Database, the largest collection of aeronautical and space science STI in the world. The Program Office is also NASA's institutional mechanism for disseminating the results of its research and development activities. These results are published by NASA in the NASA STI Report Series, which includes the following report types:

- **TECHNICAL PUBLICATION.** Reports of completed research or a major significant phase of research that present the results of NASA programs and include extensive data or theoretical analysis. Includes compilations of significant scientific and technical data and information deemed to be of continuing reference value. NASA's counterpart of peer-reviewed formal professional papers, but having less stringent limitations on manuscript length and extent of graphic presentations.
- **TECHNICAL MEMORANDUM.** Scientific and technical findings that are preliminary or of specialized interest, e.g., quick release reports, working papers, and bibliographies that contain minimal annotation. Does not contain extensive analysis.
- **CONTRACTOR REPORT.** Scientific and technical findings by NASA-sponsored contractors and grantees.

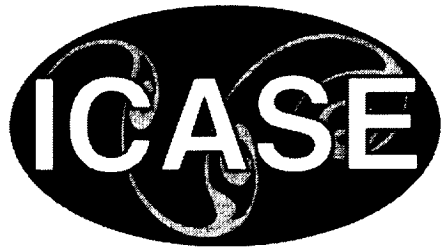
- **CONFERENCE PUBLICATIONS.** Collected papers from scientific and technical conferences, symposia, seminars, or other meetings sponsored or cosponsored by NASA.
- **SPECIAL PUBLICATION.** Scientific, technical, or historical information from NASA programs, projects, and missions, often concerned with subjects having substantial public interest.
- **TECHNICAL TRANSLATION.** English-language translations of foreign scientific and technical material pertinent to NASA's mission.

Specialized services that complement the STI Program Office's diverse offerings include creating custom thesauri, building customized data bases, organizing and publishing research results . . . even providing videos.

For more information about the NASA STI Program Office, see the following:

- Access the NASA STI Program Home Page at <http://www.sti.nasa.gov>
- Email your question via the Internet to help@sti.nasa.gov
- Fax your question to the NASA STI Help Desk at (301) 621-0134
- Telephone the NASA STI Help Desk at (301) 621-0390
- Write to:
NASA STI Help Desk
NASA Center for AeroSpace Information
7121 Standard Drive
Hanover, MD 21076-1320

NASA/CR-2002-211947
ICASE Report No. 2002-38



Analysis of Composite Skin-stiffener Debond Specimens using Volume Elements and a Shell/3D Modeling Technique

*Ronald Krueger
ICASE, Hampton, Virginia*

*Pierre J. Minguet
The Boeing Company, Philadelphia, Pennsylvania*

*ICASE
NASA Langley Research Center
Hampton, Virginia*

Operated by Universities Space Research Association



Prepared for Langley Research Center
under Contract NAS1-97046

October 2002

Available from the following:

NASA Center for AeroSpace Information (CASI)
7121 Standard Drive
Hanover, MD 21076-1320
(301) 621-0390

National Technical Information Service (NTIS)
5285 Port Royal Road
Springfield, VA 22161-2171
(703) 487-4650

ANALYSIS OF COMPOSITE SKIN-STIFFENER DEBOND SPECIMENS USING VOLUME ELEMENTS AND A SHELL/3D MODELING TECHNIQUE

RONALD KRUEGER* AND PIERRE J. MINGUET[†]

Abstract. The debonding of a skin/stringer specimen subjected to tension was studied using three-dimensional volume element modeling and computational fracture mechanics. Mixed mode strain energy release rates were calculated from finite element results using the virtual crack closure technique. The simulations revealed an increase in total energy release rate in the immediate vicinity of the free edges of the specimen. Correlation of the computed mixed-mode strain energy release rates along the delamination front contour with a two-dimensional mixed-mode interlaminar fracture criterion suggested that in spite of peak total energy release rates at the free edge the delamination would not advance at the edges first. The qualitative prediction of the shape of the delamination front was confirmed by X-ray photographs of a specimen taken during testing. The good correlation between prediction based on analysis and experiment demonstrated the efficiency of a mixed-mode failure analysis for the investigation of skin/stiffener separation due to delamination in the adherents.

The application of a shell/3D modeling technique for the simulation of skin/stringer debond in a specimen subjected to three-point bending is also demonstrated. The global structure was modeled with shell elements. A local three-dimensional model, extending to about three specimen thicknesses on either side of the delamination front was used to capture the details of the damaged section. Computed total strain energy release rates and mixed-mode ratios obtained from shell/3D simulations were in good agreement with results obtained from full solid models. The good correlations of the results demonstrated the effectiveness of the shell/3D modeling technique for the investigation of skin/stiffener separation due to delamination in the adherents.

Key words. composite materials, delamination, finite element analysis, fracture mechanics

Subject classification. Structures and Materials

1. Background. Many composite components in aerospace structures are made of flat or curved panels with co-cured or adhesively-bonded frames and stiffeners. Recent studies which focussed on the debonding mechanism included testing of skin/stiffener panels and failure analysis using shell models [1-4]. A consistent step-wise approach has been developed over the last decade which uses experiments to detect the failure mechanism, computational stress analysis to determine the location of first matrix cracking and computational fracture mechanics to investigate the potential for delamination growth. Testing of skin gage stiffened panels designed for pressurized aircraft fuselage has shown that bond failure at the tip of the frame flange is an important and very likely failure mode [5]. Comparatively simple specimens consisting of a stringer flange bonded onto a skin have been developed to study skin/stiffener debonding [6-8]. The failure that initiates at the tip of the flange in these specimens is identical to the failure observed in the full-scale panels and the frame pull-off specimens [7, 9, 10]. In a related

*ICASE, Mail Stop 132C, NASA Langley Research Center, Hampton, VA 23681-2199, (e-mail: rkrueger@icase.edu). This research was supported by the National Aeronautics and Space Administration under NASA Contract No. NAS1-97046 while the author was in residence at ICASE, NASA Langley Research Center, Hampton, VA 23681-2199.

[†] The Boeing Company, Philadelphia, Pennsylvania

study which used the same type of simulation specimen a failure criterion based on the normal strain perpendicular to the fiber direction was proposed [11].

During previous studies two-dimensional finite element models were used because modeling and computational times remain affordable, especially if many different configurations have to be analyzed during the initial design phase [9, 10, 12]. Results from a recent study where energy release rates from two-dimensional analyses were compared to data from full three-dimensional simulations indicated that plane stress and plane strain models yield upper- and lower -bound results. For more accurate predictions, however, a three-dimensional analysis is required [13, 14]. For detailed modeling and analysis of the damage observed during the experiments, therefore, the shell/3D modeling technique appears to offer a great potential for saving modeling and computational effort because only a relatively small section in the vicinity of the delamination front needs to be modeled with solid elements. The technique combines the accuracy of the full three-dimensional solution with the computational efficiency of a plate or shell finite element model and has been demonstrated for various applications [15-17]. In future applications the shell/3D modeling technique therefore is expected to be used for structural components such as stringer stiffened panels as outlined in the overview chart of Figure 1.

The first objective of this study is to complement the results of an earlier investigation of the skin/stringer debond specimen subjected to tension, where the three-dimensional mesh in the vicinity of the free edges was not fine enough to accurately capture the influence of the free edges on the distribution of the energy release rates across the width. [13, 14]. An improved mesh with a refined zone near the free edges was generated and delaminations of various lengths were discretely modeled at the locations where delaminations were observed during the experiments. Mixed mode strain energy release rates were calculated from finite element results using the virtual crack closure technique [18]. Computed strain energy release rates along the delamination front contour were used to correlate the bonding failure in the tension test configuration using a mixed-mode interlaminar fracture criterion [19, 20].

The second objective of this study is to demonstrate the use of the shell/3D modeling technique for the simulation of skin/stringer debond specimen subjected to three-point bending. A local three-dimensional model, extending to about three specimen thicknesses on either side of the delamination front was used. Delaminations of various lengths were discretely modeled at the locations where delaminations were observed during the experiments. Mixed mode strain energy release rate distributions were computed across the width of the specimens using the virtual crack closure technique. The results were compared to mixed mode strain energy release rates obtained from computations where the entire specimen had been modeled with solid elements [14].

2. Problem Description. The current study focuses on skin-stiffener debonding resulting from buckling of a thin-gage composite fuselage structure as described in reference [10]. In that study, the specimens consisted of a bonded skin and flange assembly as shown in Figure 2(a). An IM7/8552 graphite/epoxy system was used for both the skin and flange. The skin was made of prepreg tape with a measured average ply thickness of $h = 0.148$ mm and had a $[45/-45/0/-45/45/90/90/-45/45/0/45/-45]$ lay-up. The flange was made of a plain-weave fabric with a thickness of $h = 0.212$ mm. The flange lay-up was $[45/0/45/0/45/0/45]_f$, where the subscript “f” denotes fabric, “0” represents a 0° - 90° fabric ply and “45” represents a 0° - 90° fabric ply rotated by 45° . The measured bondline thickness averaged 0.178mm. Specimens were 25.4-mm wide and 177.8-mm long. The properties of the

graphite/epoxy material and the adhesive were measured at Boeing and are part of the standard design database for the V-22 tilt-rotor aircraft. Typical properties are summarized in Table 1.

Four quasi-static tension tests with a gage length of 101.6 mm were performed as shown in Figure 2(b) [10]. The value of the damage onset load was averaged from four tests and determined to be $P=17.8$ kN with a coefficient of variation of 8.9%. Three-point bending tests were performed with a bottom support span of 101.6 mm as shown in Figure 2(c). The value of the damage onset load was averaged from four tests and determined to be $Q=427.6$ N with a coefficient of variation of 12.8%. The tests were terminated when the flange debonded from the skin. Damage was documented from photographs of the polished specimen edges at each of the four flange corners identified in Figure 2(a). Corners 1 and 4 and corners 2 and 3 showed similar damage patterns for both tests. The damage at corners 2 and 3, formed first and consisted of a matrix crack in the 45° skin surface ply and a delamination at the $+45^\circ/-45^\circ$ interface as shown in Figure 3. Therefore, this damage pattern has been the focus of the current and related earlier analyses [10, 13].

Fatigue tension tests were performed at a cyclic frequency of 5 Hz, an R-ratio of 0.1 and load levels corresponding to 70%, 60%, 50% and 40% of the quasi-static damage onset load. The damage was monitored using a Questar digital microscope on one edge and an optical travelling microscope on the other edge. The specimen edges were painted white to make the cracks and delaminations more visible. Damage was documented based on location at each of the four corners identified in Figure 2(a). The number of cycles at which the first matrix crack appeared was recorded as well as the number of cycles to delamination onset. After the test, photographs of the polished specimen edges were taken under a light microscope to document the occurrence of matrix cracking and delamination. For two specimens, at intervals of damage growth, the test was stopped and the specimens removed from the grips. Photographs of the polished specimen edges were then taken under a light microscope to document the progression of the damage. The damage was found to be the same as observed for the quasi-static experiments [10].

The complex nature of the failure observed during the experiments, where the delamination changed across the specimen width from a delamination running at the skin surface $45^\circ/-45^\circ$ layer interface to a delamination propagating in the bondline above (see Figure 3), suggests the need for a three-dimensional model. The current study presents an intermediate step where three-dimensional models were created by extruding two-dimensional models across the width. The fact that the delamination changed across the specimen width from a delamination running at the skin surface $45^\circ/-45^\circ$ layer interface to a delamination propagating in the bondline above, however, is still not accounted for in this model. Nevertheless, the three-dimensional model takes width effects into account and therefore provides additional insight about the significance of edge effects.

3. Analysis of Composite Skin-Stiffener Debond Specimens Using Volume Elements. The first objective of this study was to complement the results of an earlier investigation of the skin/stringer debond specimen subjected to tension, where the three-dimensional mesh in the vicinity of the free edges was not fine enough to accurately capture the influence of the free edges on the distribution of the energy release rates across the width. [13, 14].

3.1. Three-Dimensional Finite Element Model. The deformed three-dimensional model of the specimen with load and boundary conditions is shown in Figure 4(a) for the tension load case. The specimen was modeled with ABAQUS[®] solid twenty-noded hexahedral elements C3D20R with quadratic shape functions and a reduced integration scheme. A two-dimensional mesh was made first in the x-y plane, which was then extruded across the width to create the model shown in Figure 4.

A refined mesh was used in the critical area of the 45° skin ply where cracking was observed during the tests. Outside the refined area, the mesh was modified to prevent the three-dimensional model from becoming excessively large as shown in Figure 4(b). The skin plies were grouped into three layered elements with -45/45/90, 90/-45/45 and 0/45/-45 respectively, thus taking advantage of the composite solid element option in ABAQUS[®] [21]. The fabric layers were grouped into two layered elements as shown in Figure 4(b). In the transition region at the flange several plies were modeled by one element with material properties smeared using the rule of mixtures [22]. This procedure used did not ensure the full A-B-D contribution of the plies; however, it appeared suitable for the small transition region to enforce a reasonable model size.

During earlier studies a two-dimensional model had been extruded into only ten uniformly spaced elements across the width of the specimen [13]. The final model had 32,090 elements, 145,432 nodes yielding at total of 436,296 degrees of freedom and required about eight hours of CPU time on a *SGI Origin 3200* workstation. This three-dimensional mesh, however, was not fine enough in the vicinity of the free edges ($z=0.0$ mm and $z=25.4$ mm) to accurately capture the influence of the free edges on the distribution of the energy release rates across the width. For the simulation of the tension test, therefore, the two-dimensional model was extruded into twenty elements across the width of the specimen, with a refined zone (0.74 mm, five elements) near the free edges ($z=0.0$ mm and $z=25.4$ mm) as shown in Figures 4(b) and (c). This resulted in a model with 64,180 elements and 286,104 nodes yielding at total of 858,312 degrees of freedom. The nonlinear analysis required about 29 hours of CPU time on the same workstation.

The Virtual Crack Closure Technique (VCCT) was used to calculate the mode I, II and III components of the strain energy release rates for the modeled delamination [18, 23]. For the entire investigation, the ABAQUS[®] geometric nonlinear analysis procedure was used. It was assumed that the material behaved linear elastic. This was done in accordance with previous studies which were used as reference solutions [14].

3.2. Fracture Mechanics Analysis. A fracture mechanics approach was used to investigate delamination onset once the initial crack had formed. During a series of nonlinear finite element analyses, strain energy release rates were computed at each front location for the loads applied in the experiments. A three-dimensional plot of the distribution of the energy release rate across the width of the specimen is shown in Figure 5. Values at the free edge ($z=0.0$ mm and $z=25.4$ mm) have been excluded from the plot as the model is not fine enough to accurately capture the energy release rates at the immediate edge. Along the length (x-coordinate) it was observed that after a small initial drop the computed total energy release rate increases sharply with delamination length, reaches a peak value and gradually decreases. Across the width (z-coordinate) the computed total energy release rate gradually increases with z before it first drops off near the free edges and then sharply increases in the zone of the mesh refinement in the immediate vicinity of the free edges ($z=0.0$ mm and $z=25.4$ mm).

The variation of mixed mode ratio G_S/G_T with delamination length is shown as a three-dimensional plot in Figure 6. Here G_S denotes the sum of the in-plane shearing components $G_{II}+G_{III}$, and G_T denotes the total energy release rate $G_I+G_{II}+G_{III}$, where G_I is the opening mode. For two-dimensional analyses, where $G_{III}=0$, this definition is equal to the previously used definition of the mixed mode ratio, G_{II}/G_T . For three-dimensional analysis, which also yields results for the scissoring mode G_{III} , the modified definition of G_S is introduced. A three-dimensional plot of the distribution of the mixed-mode ratio G_S/G_T across the width of the specimen is shown in Figure 6. Values at the free edge ($z=0.0$ mm and $z=25.4$ mm) have been excluded from the plot as above. Along the length (x -coordinate) it was observed that the delamination initially starts with high shearing components, followed by a drop which is equivalent to an increase in opening mode I. For longer delaminations a gradual increase in shearing components is observed. Across the width (z -coordinate) the computed mixed mode ratio indicated high shearing components near the edges, followed by a drop toward the center of the specimen, which is equivalent to an increase in opening mode I.

The distribution of the computed total energy release rate G_T across the width (z -coordinate) of the specimen is plotted in Figure 7 for the longest delamination modeled ($x=31.2$ mm). Across the width the computed total energy release rate gradually increases with z before it first drops off near the free edges and then sharply increases in the zone of the mesh refinement in the immediate vicinity of the free edges ($z=0.0$ mm and $z=25.4$ mm). Results from a previous analysis using a mesh with 10 elements uniformly spaced across the width have been included in the plot for comparison [14]. As expected the results obtained from the model with the refined mesh near the edges yield additional information about the steep increase in G_T which could not be captured with the model used earlier. The distribution of the mixed-mode ratio G_S/G_T across the width (z -coordinate) of the specimen is plotted in Figure 8 for the same location ($x=31.2$ mm). Across the width the computed mixed mode ratio shows high shearing components near the edges, followed by a drop toward the center of the specimen, which is equivalent to an increase in opening mode I. As before the results from an earlier study were included in the plot of Figure 8. The current model provided a smoother distribution across the width and yielded additional information about the steep increase in mixed-mode ratio G_T which could not be captured with the model used earlier.

3.3. Mixed-Mode Failure Investigation. Delamination onset or growth for two-dimensional problems, is predicted by comparing calculated mixed-mode energy release rate components to interlaminar fracture toughness properties measured over a range of mode mixities from pure mode I loading to pure mode II loading [24-27]. A quasi static mixed-mode fracture criterion is determined by plotting the interlaminar fracture toughness, G_c , versus the mixed-mode ratio, G_{II}/G_T , determined from data generated using pure Mode I DCB ($G_{II}/G_T=0$), pure Mode II 4ENF ($G_{II}/G_T=1$), and mixed-mode MMB tests of varying ratios, as shown in Figure 9 for IM7/8552 [20]. A curve fit of these data is performed to determine a mathematical relationship between G_c and G_{II}/G_T . [19]. Failure is expected when, for a given mixed mode ratio G_{II}/G_T , the calculated total energy release rate, G_T , exceeds the interlaminar fracture toughness, G_c . Although several specimens have also been suggested for the measurement of the mode III interlaminar fracture toughness property [28-31], an interaction criterion incorporating the scissoring shear, however, has not yet been established.

Due to the lack of an existing fracture criterion for three-dimensional problems the in-plane energy release rates G_{II} and G_{III} were combined to form the in-plane shearing component $G_S = G_{II} + G_{III}$, as suggested in [32]. Failure is now expected when, for a given mixed mode ratio G_S / G_T , the calculated total energy release rate, G_T , exceeds the interlaminar Mode I/Mode II fracture toughness, G_c . Therefore, for every computed mixed-mode ratio G_S / G_T along the delamination front as shown in Figure 8 the critical energy release rate G_c , as shown in Figure 10, can be determined using the mixed-mode delamination criterion shown in Figure 9. Next, G_T from Figure 7 was normalized by G_c and was plotted as a function of specimen width as shown in Figure 11. Along the entire front the total energy release rate G_T calculated for damage onset load is much larger than the critical value G_c ($G_T/G_c > 1$) which indicates unstable delamination growth. The critical load (P_c) which is required to advance a delamination from a pre-existing flaw is reached when G_T equals G_c ($G_T/G_c = 1$). This type of analysis to obtain the critical load (P_c) has been performed earlier using two-dimensional models to assess the effect of assumed damage and location on the delamination onset predictions for skin-stiffener debonding [33].

The focus of the current study however, was the qualitative distribution of G_T/G_c across the width of the specimen. The computed values indicate that in spite of peak total energy release rates at the free edge ($z=0.0$ mm and $z=25.4$ mm) as shown in Figures 5 and 7, the delamination is not going to advance at the edges first, because the failure criterion is a strong function of the mode mixity. The distribution suggests that the delamination will progress asymmetrically in the interior first and that a slanted front will develop from an initially straight front which was assumed in the finite element model. An increased advance is to be expected with increasing z -values. This prediction is confirmed by X-ray photographs of a specimen taken during the tension fatigue testing as shown in Figure 12. The dark areas where the contrast fluid had penetrated into the damaged section of the specimen reveal the delaminations. In Figure 12(a) the gray intensity appears to increase towards the right (increasing z -values), which suggest an increased growth in this area. This observation is confirmed by Figure 12(b) where the delamination appears to have grown further on the right side of the specimen (increasing z -values). The correlation between prediction based on analysis and experiment appears encouraging, additional detailed modeling of the three-dimensional damage however appears necessary in order to fully understand the propagation mechanism.

4. Application of a Shell/3D Modeling Technique for the Analysis of Skin/Stiffener Specimens. The objective of this study was to demonstrate the usefulness of a shell/3D modeling technique for the investigation of delamination onset from an initial crack in the skin/stringer specimen. The shell/3D modeling technique developed earlier used a local three-dimensional solid finite element model only in the immediate vicinity of the delamination front, as shown in the example of a modeled Double Cantilever Beam (DCB) specimen in Figure 13(a) [17]. The approach combined the accuracy of the full three-dimensional solution with the computational efficiency of a plate or shell finite element model. Double Cantilever Beam (DCB), End Notched Flexure (ENF), and Single Leg Bending (SLB) specimens were analyzed in an earlier study using three-dimensional finite element models to obtain reference solutions [34]. Mixed mode strain energy release rate distributions were computed across the width of the specimens using the virtual crack closure technique. The analyses were repeated using the shell/3D technique to study the feasibility for pure mode I (DCB), mode II (ENF) and mixed mode I/II (SLB) cases [17]. For a local three-dimensional model, extending to a minimum of about three specimen thicknesses on either side of the

delamination front, the results were in good agreement with mixed mode strain energy release rates obtained from computations where the entire specimen had been modeled with solid elements as shown in Figure 13(b). The shell/3D modeling technique is believed to offer a great potential for reducing the model size, since only a relatively small section in the vicinity of the delamination front needs to be modeled with solid elements. The actual efficiency is described later.

4.1. Shell/3D Finite Element Model. The deformed three-dimensional model of the specimen with load and boundary conditions is shown in Figure 14. This full three-dimensional model was used to generate the reference solutions to which the results from the shell/3D simulations were compared [14]. The specimen was modeled with ABAQUS® solid twenty-noded hexahedral elements C3D20R with quadratic shape functions and a reduced integration scheme. To create the model, a two-dimensional mesh was extruded into ten elements across the width of the specimen as shown in Figure 14(a). A detail of the modeled delaminated region is shown in Figure 14(b). For short delamination lengths ($a < 1.0$ mm) crack opening mode I was apparent. For longer delaminations mode I ceased and the surfaces started to overclose as shown in the detail of Figure 14(c). This phenomenon had not been observed in the earlier results from two-dimensional analyses [33].

The deformed shell/3D model of the specimen is shown in Figure 15(a). The global section was modeled with ABAQUS® reduced integrated eight-noded quadrilateral shell elements S8R. The local three-dimensional model extended to about three specimen thicknesses on either side of the delamination front as shown in Figure 15(b). This configuration yielded good results during the initial feasibility study shown in Figure 13 [17]. The local three-dimensional section was modeled with solid C3D20R elements and was almost identical to the equivalent segment of the full three-dimensional model shown in Figure 14. A refined three-dimensional mesh was used in the critical area of the 45° skin ply where cracking was observed during the tests as shown in Figure 15(c). Outside the refined area, the mesh was modified to prevent the three-dimensional model from becoming excessively large. The skin plies were grouped into four layered elements with 45/-45/0, -45/45/90, 90/-45/45 and 0/45/-45 respectively, thus taking advantage of the composite solid element option in ABAQUS® [21]. The fabric layers and the resin layer were grouped into five layered elements. In the transition regions several plies were modeled by one element with material properties smeared using the rule of mixtures [22]. This procedure did not ensure the full A-B-D contribution of the plies; however, it appeared suitable for the small transition regions to enforce a reasonable model size. The transition from the global shell element model to the local three-dimensional model in the vicinity of the delamination front was accomplished by using multi-point constraint options given by ABAQUS® to enforce appropriate translations and rotations at the shell-solid interface [21]. Using the shell/3D approach the total number of freedoms could be reduced by more than 12% compared to the full three-dimensional model of the skin/stringer specimen.

The shell/3D model shown in Figure 15, however, was not fine enough in the vicinity of the free edges ($z=0.0$ mm and $z=25.4$ mm) to accurately capture the influence of the free edges on the distribution of the energy release rates across the width. Therefore, a shell/3D model as shown in Figure 16 was created with twenty elements across the width of the specimen corresponding to the full three-dimensional model shown in Figure 4. The new

shell/3D model was improved by a refined zone (0.74 mm, five elements) near the free edges ($z=0.0$ mm and $z=25.4$ mm) as shown in Figures 16(b) and (c). The efficiency is discussed in the summary.

The Virtual Crack Closure Technique (VCCT) was used to calculate the mode I, II and III components of the strain energy release rates for the modeled delamination [18, 23]. For the entire investigation, the ABAQUS[®] geometric nonlinear analysis procedure was used. This was done in accordance with previous studies which were used as reference solutions [14].

4.2. Global Response. First, the global response of the specimens was computed at the mean quasi-static damage onset load determined from experiments. The load-displacement and the load-strain behavior computed from different FE models were compared to the corresponding experimental results. This global response was used to examine whether the FE models, the boundary conditions, the loads and the material properties used in the model yielded reasonable results. Strains were averaged from computed nodal point values over a length corresponding to the dimensions of the strain gages shown in Figure 2(a) [10].

The load versus displacement plot in Figure 17 shows that shell/3D model exhibits a stiffer behavior compared to results from the full three-dimensional model. The models also show a slightly stiffer response compared to the experiments (DCDT). This discrepancy may be explained by the fact that the material data used in the FE simulation originated from the literature. For a consistent simulation, material data should be taken from the batch of material that was used to manufacture the specimens. For comparison, results from 2D analysis were included in the plot of Figure 17 [14]. Results from the plane-strain analysis indicated a stiffer behavior as expected. This is caused by the constraints inherent to the plane-strain model, particularly in the $\pm 45^\circ$ plies. The plane-stress model which imposes the out of plane stresses to be zero and allows the displacement to be the free parameter exhibits – as expected - a more compliant behavior. The influence of the assumptions made in developing two-dimensional finite element models on skin-stiffener debonding specimens was studied in detail in [14] where geometrically nonlinear finite element analyses using two-dimensional plane-stress and plane-strain elements as well as three different generalized plane strain type approaches were performed.

A comparison of measured strains at the surface of the flange (see Figure 2(a)) and computed results is shown in Figure 18. In Figure 19, measured strains at the surface of the top 45° skin ply near the flange tip (see Figure 2(a)) and computed surface strains were compared. For both locations, the strains calculated from the shell/3D model are in good agreement with the results from the full three-dimensional finite element model. The models show a slightly stiffer response compared to the strains measured during the experiments. As before, results from 2D analysis were included in the plots of Figure 18 and 19 for comparison [14]. The plane-strain model showed a stiffer behavior yielding an upper bound while the plane-stress models were more compliant yielding a lower bound.

4.3. Fractures Mechanics Analysis. The objective of this study was to demonstrate the usefulness of the shell/3D modeling technique for the investigation of delamination onset from an initial crack. A fracture mechanics approach was used and during a series of nonlinear finite element analyses, strain energy release rates were computed at each front location for the loads applied in the experiments. Results obtained from the shell/3D model are

presented in Figure 20 as a three-dimensional plot of the distribution of the total energy release rate, G_T , across the width of the specimen. Values at the free edge ($z=0.0$ mm and $z=25.4$ mm) have been excluded from the plots as the model was not fine enough to accurately capture the influence of the free edges on the distribution of the energy release rates. Unlike the tension loading case it was observed that G_T increases continuously along the length (x -coordinate), except for the zones near the free edges ($z=0.0$ mm and $z=25.4$ mm) where a sharp decrease is observed caused by the overclosure of the interfaces after about 1 mm of delamination growth. The continuous increase of G_T along the length indicates unstable delamination growth. Across the width (z -coordinate) the computed total energy release rate gradually increases with z before it drops off near the free edge ($z=25.4$ mm).

A three-dimensional plot of the distribution of mixed mode ratio G_S/G_T with delamination length is shown in Figure 21. Here G_S denotes the sum of the in-plane shearing components $G_{II}+G_{III}$, and G_T denotes the total energy release rate $G_I+G_{II}+G_{III}$, where G_I is the opening mode. For two-dimensional analyses, where $G_{III}=0$, this definition is equal to the commonly used definition of the mixed mode ratio, G_{II}/G_T . For three-dimensional analysis, which also yields results for the scissoring mode G_{III} , the modified definition of G_S is introduced. As before, values at the free edge ($z=0.0$ mm and $z=25.4$ mm) have been excluded from the plots as the model was not fine enough to accurately capture the influence of the free edges on the distribution of the energy release rates. Along the length (x -coordinate) it was observed that the delamination initially starts with high shearing components, followed by a drop which is equivalent to an increase in opening mode I. For longer delaminations the shearing component remains constant. Unlike the tension loading case, the mixed mode ratio rises sharply at the edges for delaminations longer than 1 mm. This is caused by the overclosure of the delaminated surface near the edges of the model where the crack opening mode I disappears. A detailed study of this phenomenon would require contact analysis and preferably a refined model near the free edges.

The total energy release rates along the centerline of the specimen ($z=12.7$ mm) obtained from three-dimensional and shell/3D analysis are plotted in Figure 22 for comparison. The values from the shell/3D analysis are within 6% of the results obtained from the full three-dimensional simulations. Improved results may be obtained by enlarging the section modeled with solid elements. The values from previous plain strain and plane stress analysis were included in Figure 22 for comparison [14]. Qualitatively all results follow the same trend. As before the values from plane strain and plane stress analysis form upper and lower bounds, except for very short delamination lengths.

The variation of mixed mode ratio G_S/G_T with delamination length is shown in Figure 23. For short delamination length the mixed mode ratio yields high shearing components, followed by a drop which is equivalent to an increase in opening mode I. For longer delaminations the shearing component remains constant. The values from the shell/3D analysis are in good agreement with the results obtained from the full three-dimensional simulations. The values from previous plain strain and plane stress analysis were included in Figure 23 for comparison and follow the same trend [14]. The results from three-dimensional analysis in the center of the specimen width ($z=12.7$ mm) show a higher shearing component compared to the results from two-dimensional analysis.

The distribution of the computed total energy release rate G_T across the width (z -coordinate) of the specimen is plotted in Figure 24 for the longest delamination modeled ($x=31.2$ mm). Across the width the computed total energy release rate gradually increases with z before it drops off near the free edge ($z=25.4$ mm). Results from a previous analysis obtained from the full three-dimensional model shown in Figure 14 have been included in the plot for comparison [14]. The G_T values from the shell/3D analysis are 6% lower than the results obtained from the full three-dimensional simulations. The distribution of the mixed-mode ratio G_S/G_T across the width (z -coordinate) of the specimen is plotted in Figure 25 for the same location ($x=31.2$ mm). Across the width the computed mixed mode ratio shows an almost constant value with increasing shearing components near the edges ($z=0.0$ mm and $z=25.4$ mm).

For the longest delamination modeled ($x=31.2$ mm), the distribution of the computed total energy release rate G_T across the width (z -coordinate) of the specimen is plotted in Figure 26. Results were obtained from the shell/3D model with a refined mesh near the edges as shown in Figure 16. Across the width, the computed total energy release rate gradually increases before it first drops off near the free edges and then sharply increases in the zone of the mesh refinement in the immediate vicinity of the free edges ($z=0.0$ mm and $z=25.4$ mm). As expected, the results obtained from the model with the refined mesh near the edges yield additional information about the steep increase in G_T which could not be captured with the less refined models (Figure 24). The distribution of the mixed-mode ratio G_S/G_T across the width (z -coordinate) of the specimen is plotted in Figure 27 for the same location ($x=31.2$ mm). Across the width the computed mixed mode ratio is nearly constant and dominated by opening mode I but shows high shearing components near the edges which is caused by the overclosure of the delaminated surface near the edges where the crack opening mode I disappears. The current model provided a smoother distribution across the width and yielded additional information about the steep increase in mixed-mode ratio G_T which could not be captured with the less refined model (Figure 25).

A mixed-mode failure investigation as for the tension load case (see section 3.3) was not performed for the bending load case due to the lack of information regarding the size and shape of the delamination propagation. Further, a detailed study would also require additional contact analysis to avoid overclosure at the edges of the specimen during the simulations.

4.4. Summary. Computed total strain energy release rates and mixed mode ratios obtained from shell/3D simulations were in good agreement with results obtained from full solid models. The concurrence of the results demonstrated the effectiveness of the shell/3D modeling technique for the investigation of delamination onset from an initial crack. However, for the current configuration a desired reduction in computation time could not be achieved. This is partially caused by the fine three-dimensional mesh in the vicinity of the delaminated region, which was not replaced by shell elements. Additionally, the transition from the global shell element model to the local three-dimensional model was accomplished by multi-point constraints to enforce appropriate translations and rotations at the shell-solid interface, which increased the computational effort. Nevertheless, for large built-up composite structures modeled with plate elements, the shell/3D modeling technique offers a great potential for reducing the model size, compared to a full three-dimensional model. In future applications the shell/3D modeling

technique will therefore progress towards structural components such as stringer stiffened panels as outlined in the overview chart of Figure 1.

5. Concluding Remarks. The debonding of a skin/stringer specimen subjected to tension was studied using three-dimensional volume element modeling and computational fracture mechanics. A three-dimensional finite element model with a refined zone near the free edges was generated and delaminations of various lengths were discretely modeled at the locations where delaminations were observed during the experiments. The goal was to complement the results of an earlier investigation where the three-dimensional mesh in the vicinity of the free edges had not been fine enough to accurately capture the influence of the free edges on the distribution of the energy release rates across the width.

Mixed mode strain energy release rates were calculated from finite element results using the virtual crack closure technique. The simulations revealed an increase in total energy release rate in the immediate vicinity of the free edges of the specimen which had not been captured by earlier models. The results also yielded an increase in shearing mode towards the free edge. Correlation of the computed mixed-mode strain energy release rates along the delamination front contour with a two-dimensional mixed-mode interlaminar fracture criterion became possible by introducing the in-plane shearing component $G_S = G_{II} + G_{III}$, and defining the mixed mode ratio as G_S / G_T compared instead of the traditional two-dimensional definition of G_{II} / G_T . The approach suggested that in spite of peak total energy release rates at the free edge the delamination would not advance at the edges first because the failure criterion is a strong function of mode mixity. The qualitative prediction of the shape of the delamination front was confirmed by X-ray photographs of a specimen taken during testing. The good correlation between prediction based on analysis and experiment is encouraging future investigations.

The application of the shell/3D modeling technique for the simulation of skin/stringer debond specimen subjected to three-point bending was also demonstrated. The study extended the application of this technique beyond the simulation of simple specimens – such as DCB, ENF and SLB specimens – where the delamination is located between unidirectional plies in the mid-plane of the specimen. The global structure was modeled with shell elements. A three-dimensional model, extending to about three specimen thicknesses on either side of the delamination front was used locally. Delaminations of various lengths were discretely modeled at the locations where delaminations were observed during previous experiments.

Computed strains at the center of the flange were compared with results obtained from full three-dimensional finite element analysis and experimental data. Results from both analyses and experiment were in good agreement. Calculated total strain energy release rates and mixed mode ratios obtained from shell/3D simulations also were in good agreement with results obtained from full solid models. The concurrence of the results demonstrated the effectiveness of the shell/3D modeling technique for the investigation of delamination onset from an initial crack. For comparison results from plane stress and plane strain models provided flange strains, as well as energy release rates, which formed an upper and lower bound of the results obtained from full three-dimensional or shell/3D simulations.

The current study provided an additional verification step for the technique prior to its application to large, full-scale stringer stiffened panels because failure observed in the skin/stringer specimen is identical to the failure observed in the full-scale panels where the delamination is located between plies of different orientation. For large built-up composite structures modeled with plate elements, the shell/3D modeling technique offers a great potential for reducing the model size, compared to a full three-dimensional model, since only a relatively small section in the vicinity of the delamination front needs to be modeled with solid elements.

Acknowledgements. The authors gratefully acknowledge Drs. T. Kevin O'Brien and Isabelle Paris for providing insight and experimental results on the specimens analyzed in this paper.

REFERENCES

- [1] I. S. RAJU, R. SISTLA and T. KRISHNAMURTHY, *Fracture Mechanics Analyses for Skin-Stiffener Debonding*, Eng. Fracture Mech., 54 (1996), pp. 371-385.
- [2] E. H. GLAESSGEN, I. S. RAJU and C. C. POE, *Fracture Mechanics Analysis of Stitched Stiffener-Skin Debonding*, The 39th AIAA/ASME/ASCE/AHS/ASC Structures, Structural Dynamics and Materials Conference, Long Beach, California, AIAA 98-2022, April 20-23, 1998.
- [3] B. G. FALZON, G. A. O. DAVIES and E. GREENHALGH, *Failure of thick-skinned stiffener runout sections loaded in uniaxial compression*, Composite Structures, 53 (2001), pp. 223-233.
- [4] J. W. H. YAP, M. L. SCOTT, R. S. THOMSON and D. HACHENBERG, *The analysis of skin-to-stiffener debonding in composite aerospace structures*, Composite Structures, 57 (2002), pp. 425-435.
- [5] P. J. MINGUET, M. J. FEDRO, T. K. O'BRIEN, R. H. MARTIN and L. B. ILCEWICZ, *Development of a Structural Test Simulating Pressure Pillowing Effects in Bonded Skin/Stringer/Frame Configuration*, Proceedings of the 4th NASA/DoD Advanced Composite Technology Conference, Salt Lake City, Utah, 1993.
- [6] P. J. MINGUET and T. K. O'BRIEN, *Analysis of Composite Skin/Stringer Bond Failures Using a Strain Energy Release Rate Approach*, in A. Poursartip and K. Street, eds., The 10th International Conference on Composite Materials, 1995, pp. 245-252.
- [7] P. J. MINGUET and T. K. O'BRIEN, *Analysis of Test Methods for Characterizing Skin/Stringer Debonding Failures in Reinforced Composite Panels*, Composite Materials: Testing and Design (12th Volume), ASTM STP 1274, 1996, pp. 105-124.
- [8] P. J. MINGUET, *Analysis of the Strength of the Interface Between Frame and Skin in a Bonded Composite Fuselage Panel*, The 38th AIAA/ASME/ASCE/AHS/ASC Structures, Structural Dynamics and Materials Conference, 1997, pp. 2783-2790.
- [9] R. KRUEGER, M. K. CVITKOVICH, T. K. O'BRIEN and P. J. MINGUET, *Testing and Analysis of Composite Skin/Stringer Debonding Under Multi-Axial Loading*, J. Composite Materials, 34 (2000), pp. 1263-1300.
- [10] R. KRUEGER, I. L. PARIS, T. K. O'BRIEN and P. J. MINGUET, *Fatigue Life Methodology for Bonded Composite Skin/Stringer Configurations*, Journal of Composites Technology and Research, 24 (2002), pp. 308-331.
- [11] J. VAN RIJN, *Failure Criterion for the Skin-Stiffener Interface in Composite Aircraft Panels*, Proceedings of the ASC 13th Annual Technical Conference on Composite Materials, 1998, pp. 1064-1093.
- [12] I. L. PARIS, R. KRUEGER and T. K. O'BRIEN, *Effect of Assumed Damage and Location on the Delamination Onset Predictions for Skin-Stiffener Debonding*, AHS International Structures Specialists' Meeting, Williamsburg, Virginia, October 30 - November 1, 2001.
- [13] R. KRUEGER, I. L. PARIS, T. K. O'BRIEN and P. J. MINGUET, *Comparison of 2D Finite Element Modeling Assumptions with Results from 3D Analysis for Composite Skin-Stiffener Debonding*, Composite Structures, 57 (2002), pp. 161-168.
- [14] R. KRUEGER and P. J. MINGUET, *Influence of 2D Finite Element Modeling Assumptions on Debonding Prediction For Composite Skin-Stiffener Specimens Subjected to Tension and Bending*, NASA/CR-2002-211452, ICASE Report No. 2002-4, 2002.

- [15] C. G. DÁVILA, *Solid-to-Shell Transition Elements for the Computation of Interlaminar Stresses*, Computing Systems in Engineering, 5 (1994), pp. 193-202.
- [16] J. T. WANG, C. G. DÁVILA, D. W. SLEIGHT and T. KRISHNAMURTHY, *Crown Panel Stiffener-Frame Intersection Structural Integrity Analyses*, 5th NASA/DoD Conference on Advanced Composites Technology, Seattle, Washington, 1994.
- [17] R. KRUEGER and T. K. O'BRIEN, *A Shell/3D Modeling Technique for the Analysis of Delaminated Composite Laminates*, Composites Part A: Applied Science and Manufacturing, 32 (2001), pp. 25-44.
- [18] E. F. RYBICKI and M. F. KANNINEN, *A Finite Element Calculation of Stress Intensity Factors by a Modified Crack Closure Integral*, Eng. Fracture Mech., 9 (1977), pp. 931-938.
- [19] T. K. O'BRIEN, *Interlaminar fracture toughness: The long and winding road to standardization*, Composites Part B, 29 (1998), pp. 57-62.
- [20] P. HANSEN and R. MARTIN, *DCB, 4ENF and MMB Delamination Characterisation of S2/8552 and IM7/8552*, UK N68171-98-M-5177, Materials Engineering Research Laboratory Ltd. (MERL), Hertford, UK, 1999.
- [21] *ABAQUS/Standard - User's Manual - Version 5.6*, Hibbitt, Karlsson & Sorensen, Inc., 1996.
- [22] S. W. TSAI and H. T. HAHN, *Introduction to Composite Materials*, Technomic Publishing Co., Inc., 1980.
- [23] R. KRUEGER, *The Virtual Crack Closure Technique: History, Approach and Applications*, NASA/CR-2002-211628, ICASE Report No. 2002-10, 2002.
- [24] *ASTM D 5528-94a, Standard Test Method for Mode I Interlaminar Fracture Toughness of Unidirectional Fiber-Reinforced Polymer Matrix Composites*, Annual Book of ASTM Standards, American Society for Testing and Materials, 2000.
- [25] R. H. MARTIN and B. D. DAVIDSON, *Mode II Fracture Toughness Evaluation Using A Four Point Bend End Notched Flexure Test*, Plastics, Rubber and Composites, 28 (1999), pp. 401-406.
- [26] *ASTM D 6671-01, Standard Test Method for Mixed Mode I-Mode II Interlaminar Fracture Toughness of Unidirectional Fiber Reinforced Polymer Matrix Composites*, Annual Book of ASTM Standards, American Society for Testing and Materials, 2000.
- [27] J. R. REEDER, *A Bilinear Failure Criterion for Mixed-Mode Delamination*, Composite Materials: Testing and Design (Eleventh Volume), ASTM STP 1206, American Society for Testing and Materials, 1993, pp. 303-322.
- [28] S. M. LEE, *Failure Mechanics of Edge Delamination of Composites*, J. Composite Mat., 24 (1990), pp. 1200-1212.
- [29] R. H. MARTIN, *Evaluation of the Split Cantilever Beam for Mode III Delamination Testing*, Composite Materials: Fatigue and Fracture (3rd Volume), ASTM STP 1110, 1991, pp. 243-266.
- [30] P. ROBINSON and D. Q. SONG, *Development of an improved mode III delamination test for composites*, Composites Science and Technology, 52 (1994), pp. 217-233.
- [31] J. LI, S. M. LEE, E. W. LEE and T. K. O'BRIEN, *Evaluation of the Edge Crack Torsion ECT Test for Mode III Interlaminar Fracture Toughness of Laminated Composites*, Journal of Composites Technology and Research, 19 (1997), pp. 174-183.
- [32] M. KÖNIG, R. KRÜGER, K. KUSSMAUL, M. V. ALBERTI and M. GÄDKE, *Characterizing Static and Fatigue Interlaminar Fracture Behaviour of a First Generation Graphite/Epoxy Composite*, in S. J. Hooper, ed., Composite Materials: Testing and Design - (13th Vol.), ASTM STP 1242, American Society for Testing and Materials, 1997, pp. 60-81.
- [33] I. L. PARIS, R. KRUEGER and T. K. O'BRIEN, *Effect of Assumed Damage and Location on the Delamination Onset Predictions for Skin-Stiffener Debonding*, AHS Journal, submitted (2002).
- [34] R. KRUEGER and T. K. O'BRIEN, *A Shell/3D Modeling Technique for the Analysis of Delaminated Composite Laminates*, NASA/TM-2000-210287, ARL-TR-2207, 2000.

TABLE 1.
Material Properties

IM7/8552 Unidirectional Graphite/Epoxy Prepreg		
$E_{11} = 161.0 \text{ GPa}$	$E_{22} = 11.38 \text{ GPa}$	$E_{33} = 11.38 \text{ GPa}$
$\nu_{12} = 0.32$	$\nu_{13} = 0.32$	$\nu_{23} = 0.45$
$G_{12} = 5.17 \text{ GPa}$	$G_{13} = 5.17 \text{ GPa}$	$G_{23} = 3.92 \text{ GPa}$
IM7/8552 Graphite/Epoxy Plain Weave Fabric		
$E_{11} = 71.7 \text{ GPa}$	$E_{22} = 71.7 \text{ GPa}$	$E_{33} = 10.3 \text{ GPa}$
$\nu_{12} = 0.04$	$\nu_{13} = 0.35$	$\nu_{23} = 0.35$
$G_{12} = 4.48 \text{ GPa}$	$G_{13} = 4.14 \text{ GPa}$	$G_{23} = 4.14 \text{ GPa}$
Grade 5 FM300 Adhesive		
$E = 1.72 \text{ GPa}$	$\nu = 0.3$	(assumed isotropic)

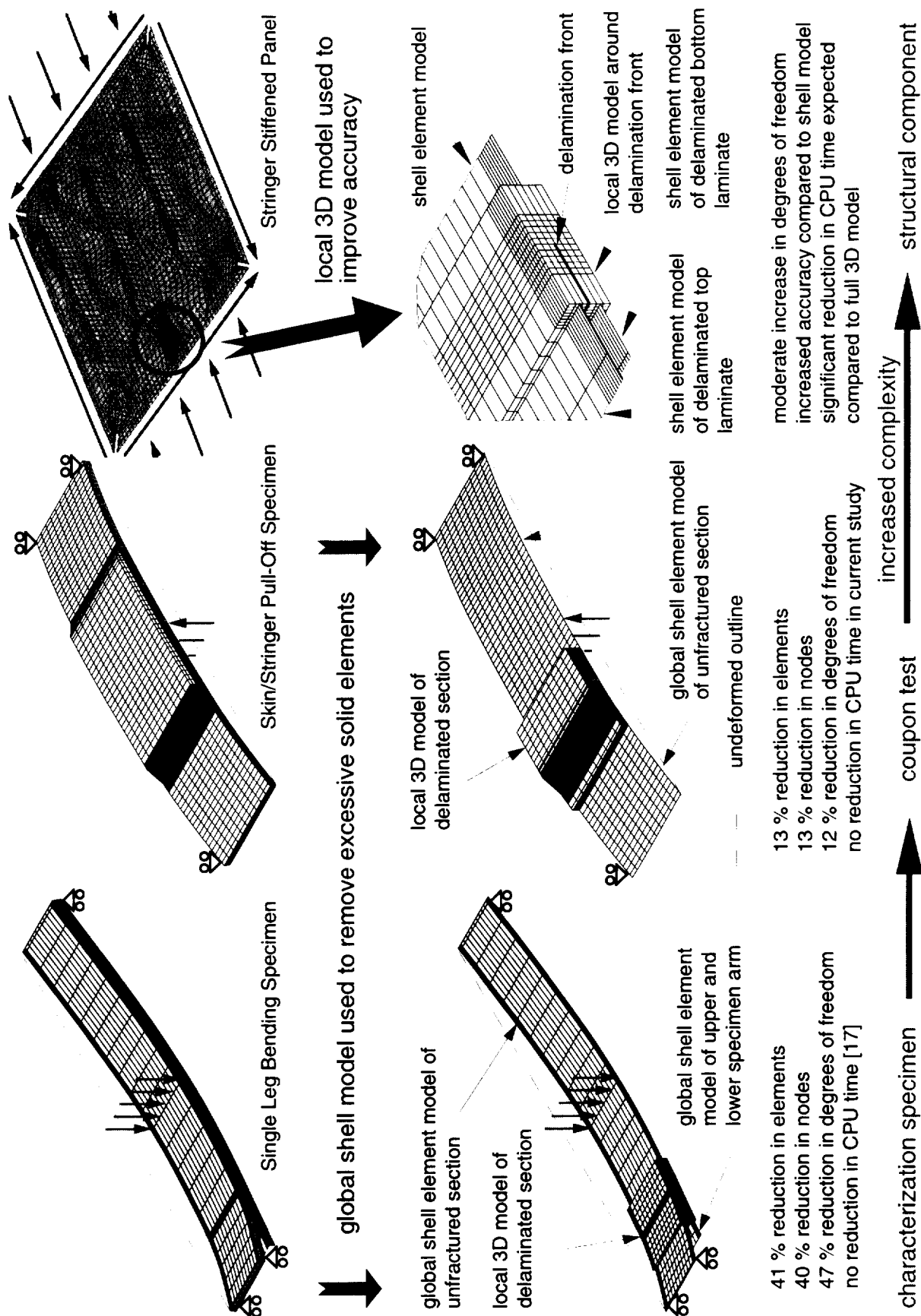
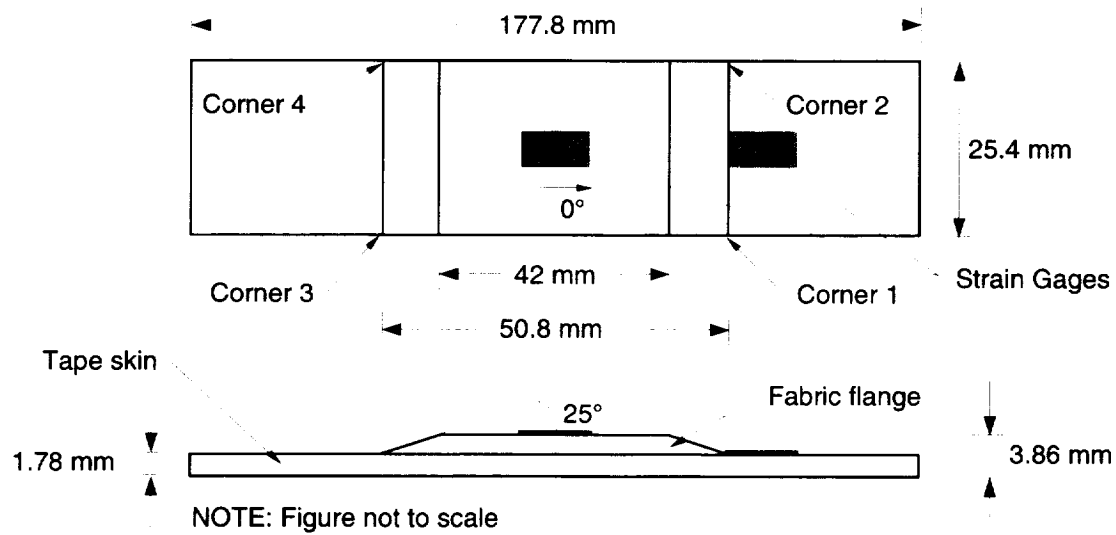
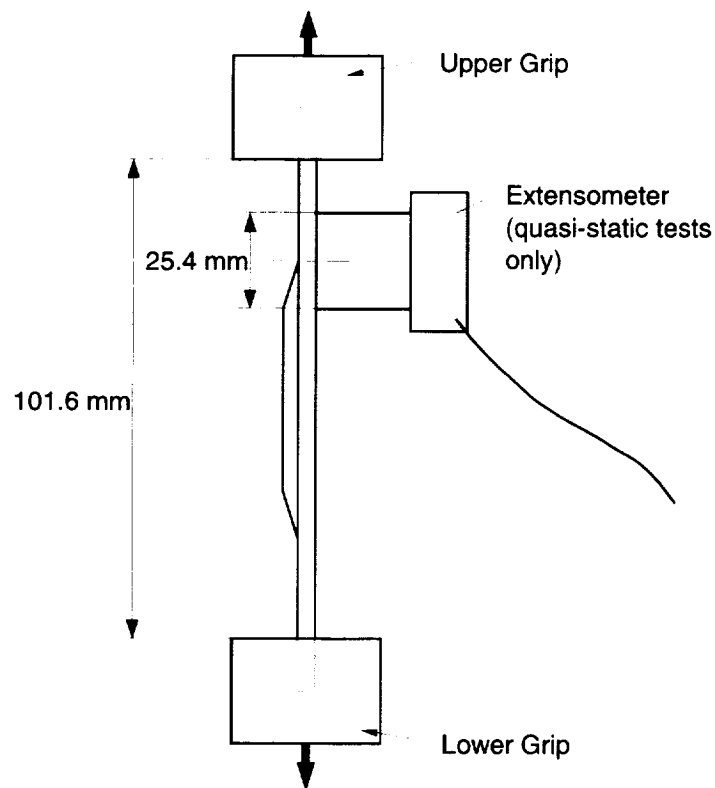


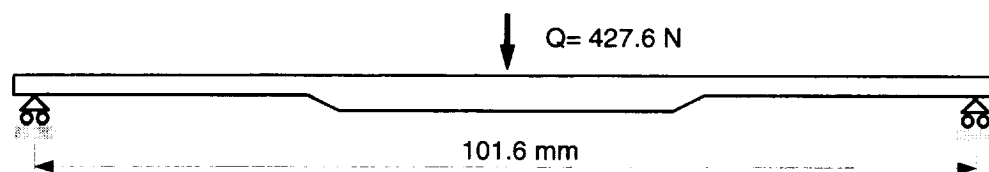
FIGURE 1. Application of the shell/3D modeling technique



(a) Specimen configuration



(b) Tension test set-up



(c) Three-point bending case

FIGURE 2. Specimen configuration and test set-up.

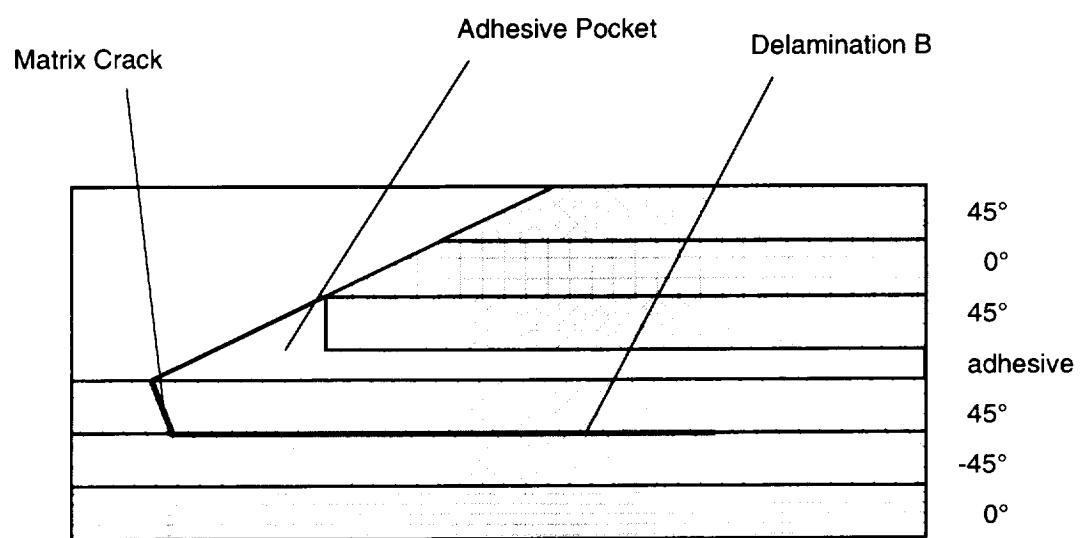


FIGURE 3. Typical damage patterns at specimen corners 2 and 3 [10]

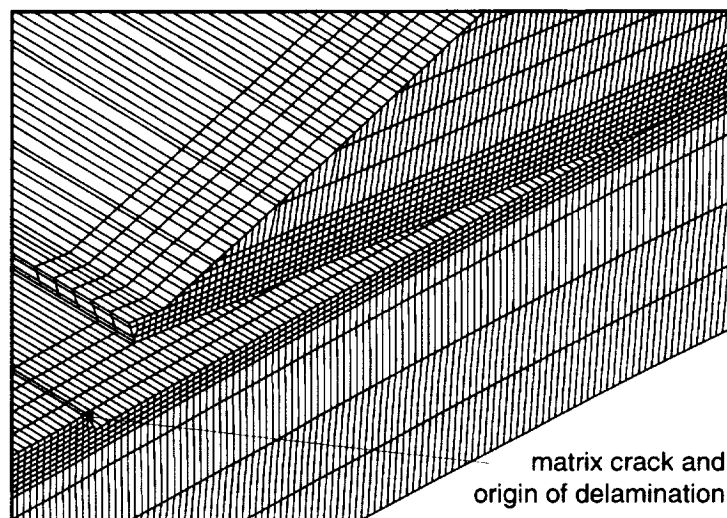
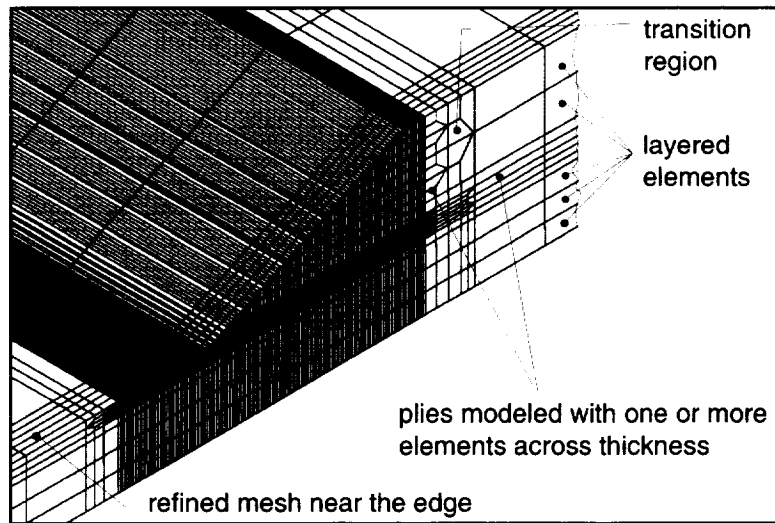
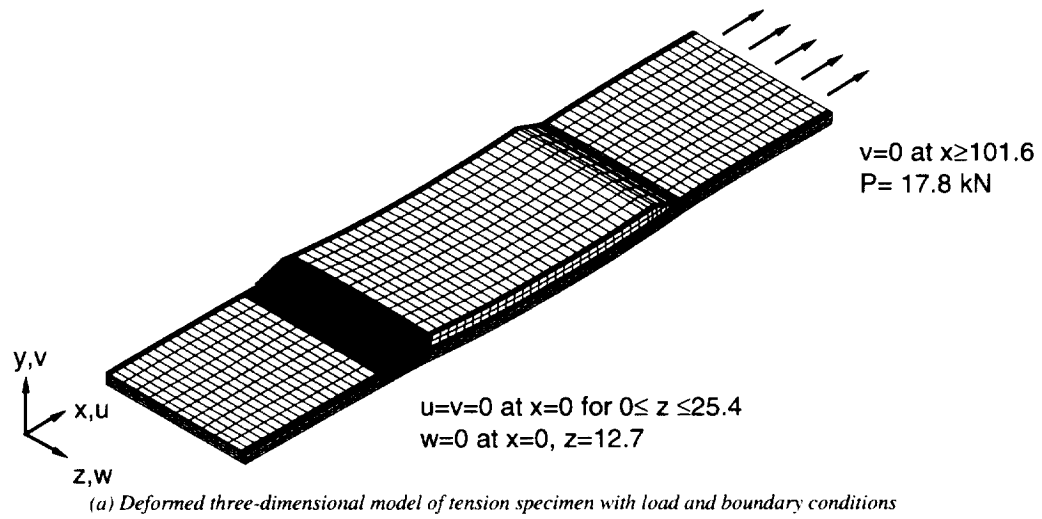


FIGURE 4. Full three-dimensional model of skin/flange specimen

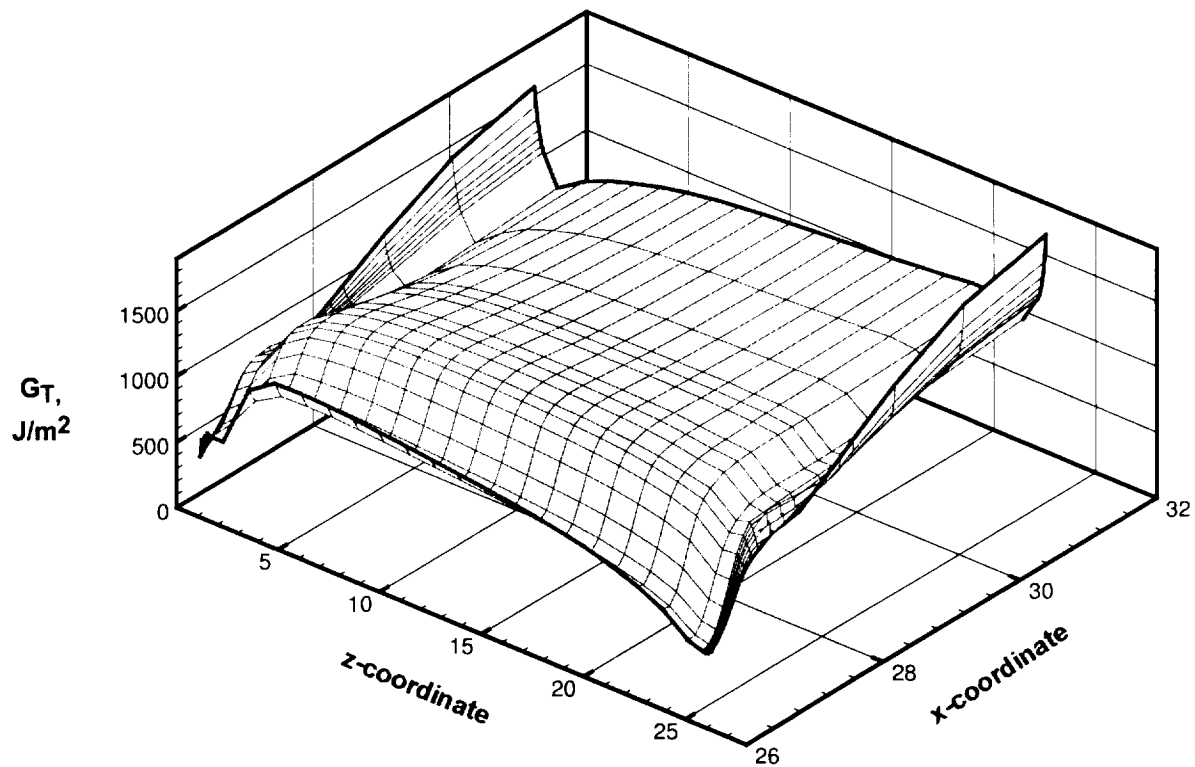


FIGURE 5. Computed total energy release rate distribution for tension test.

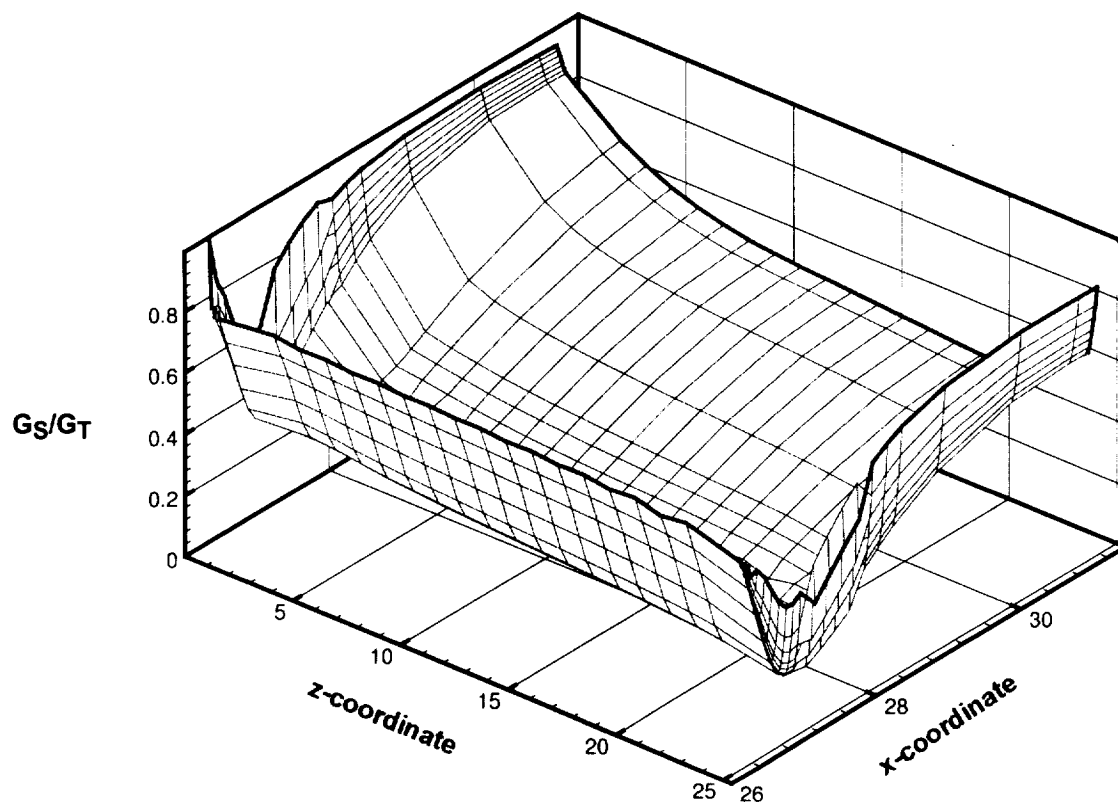


FIGURE 6. Computed mixed mode ratio G_S/G_T for tension test.

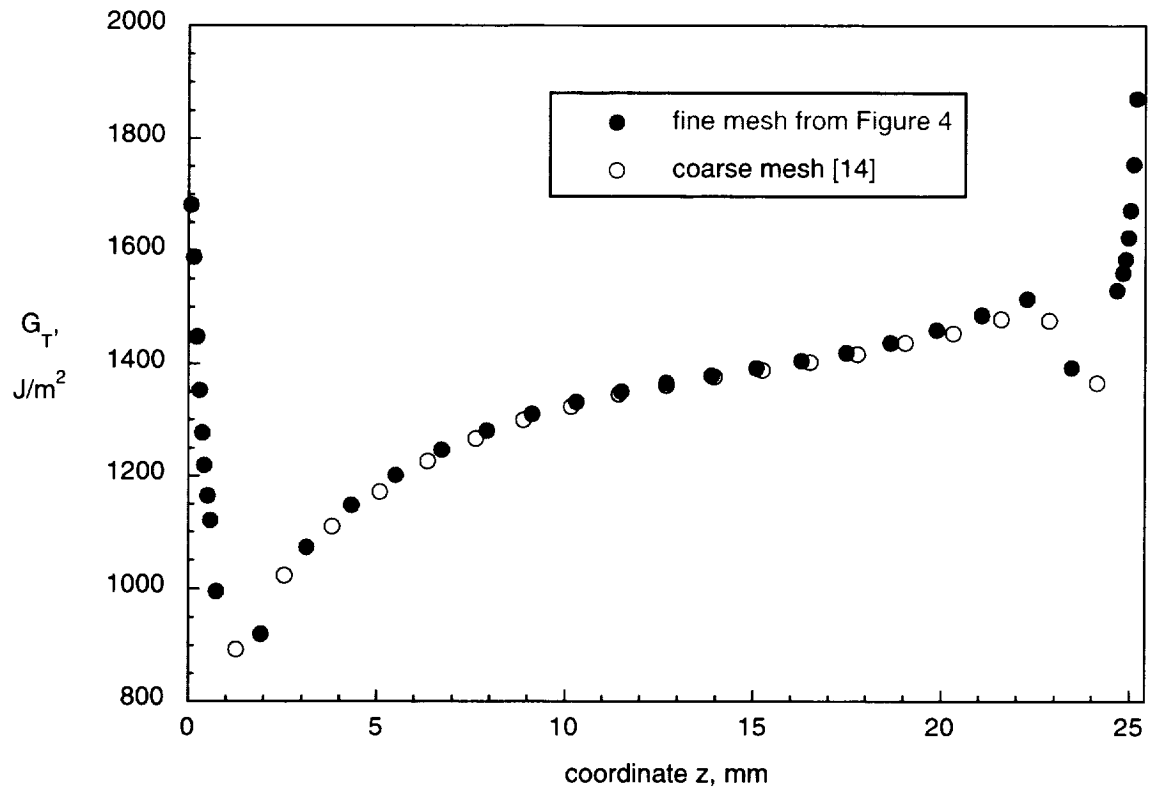


FIGURE 7. Computed total energy release rate across the width of the specimen at $x = 31.2$ mm for tension test

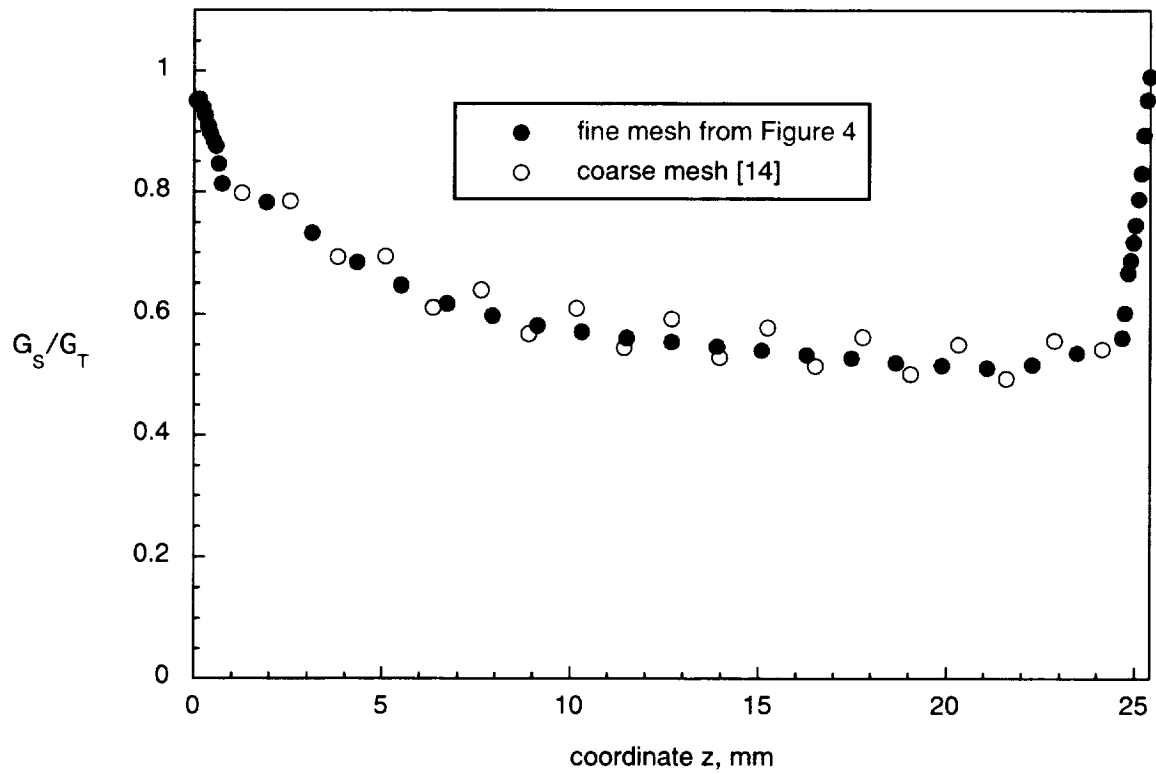


FIGURE 8. Computed mixed-mode ratio across the width of the specimen at $x = 31.2$ mm for tension test

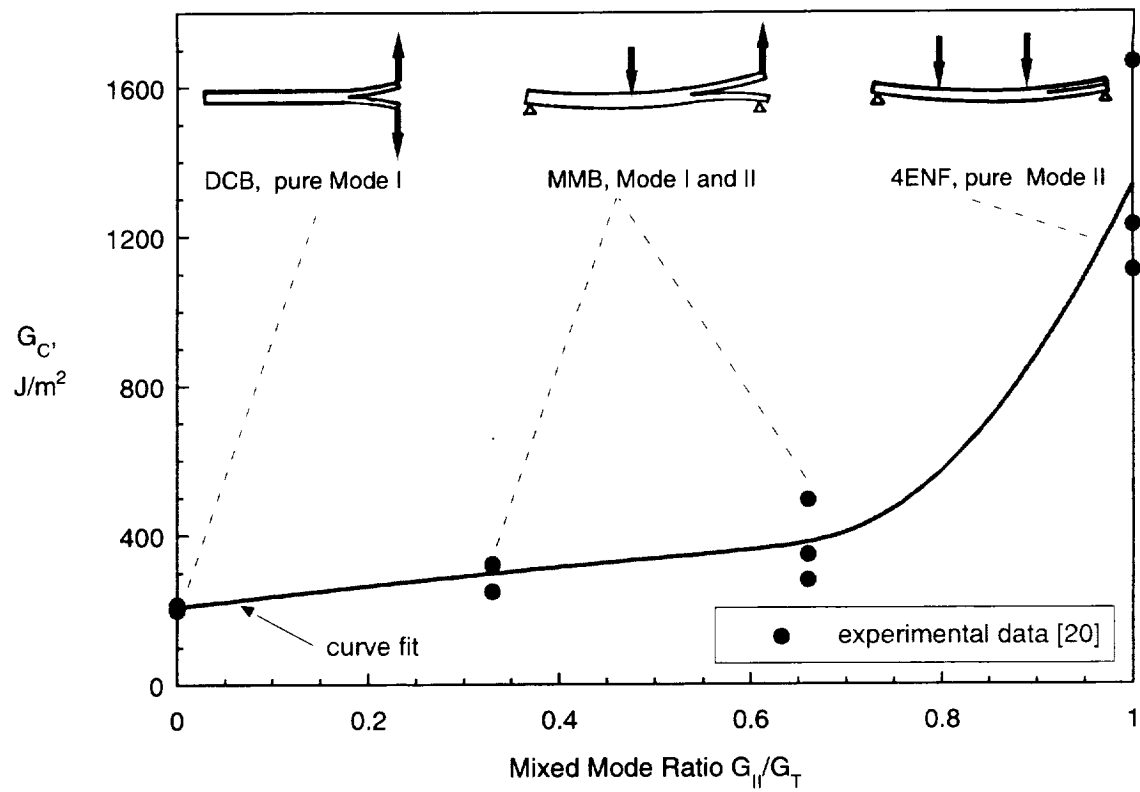


FIGURE 9. Mixed-mode delamination criterion for IM7/8552.

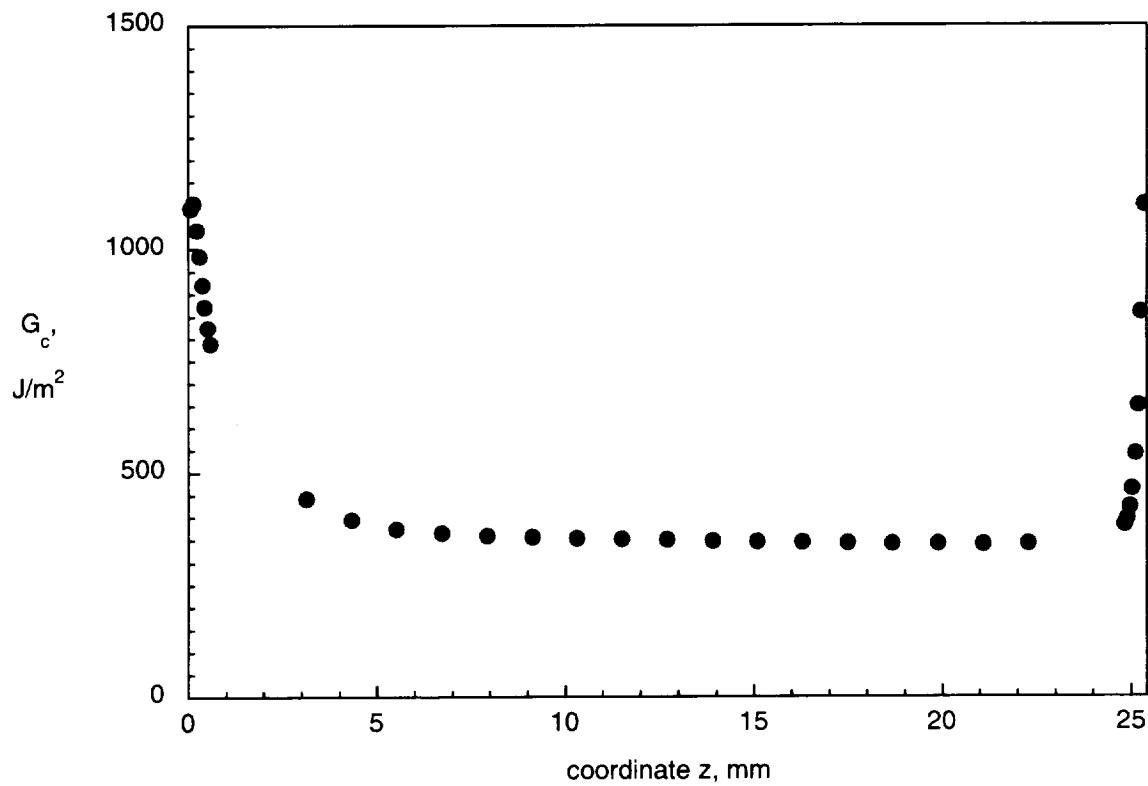


FIGURE 10. Critical total energy release rate across the width of the specimen at $x = 31.2$ mm for tension test

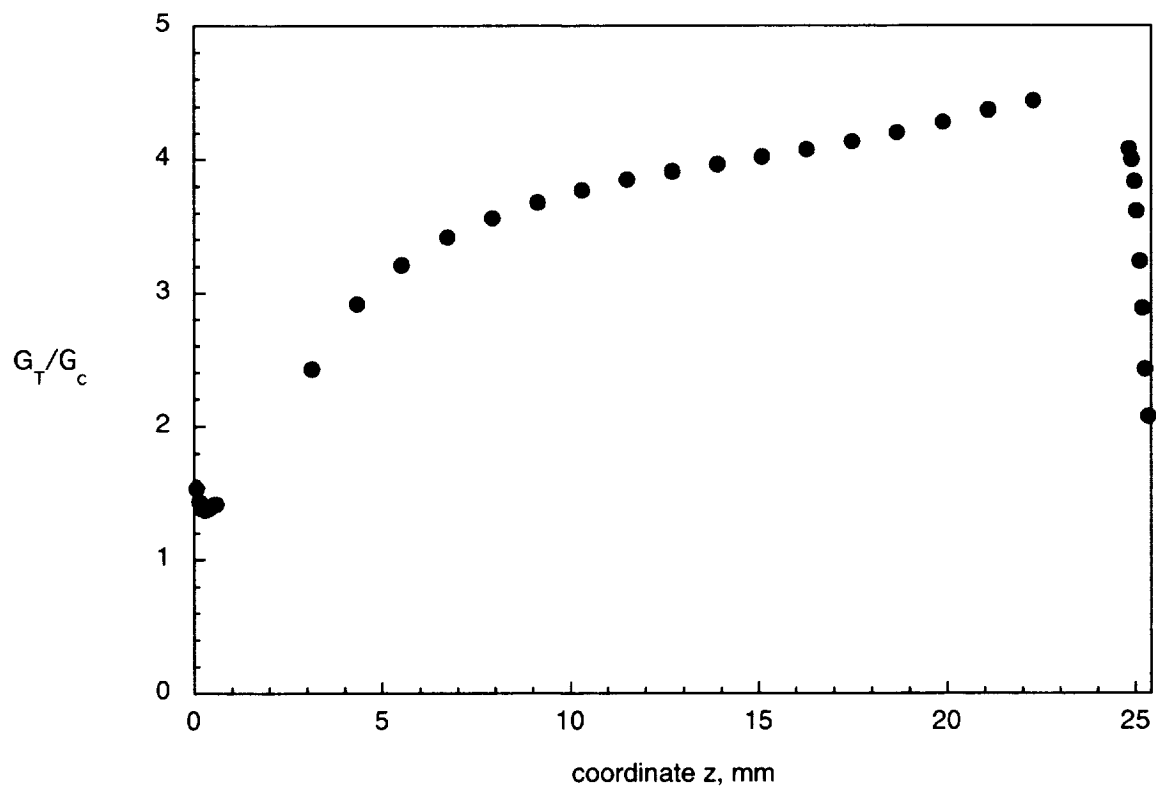


FIGURE 11. Failure ratio G_T/G_c across the width of the specimen at $x = 31.2$ mm for tension test

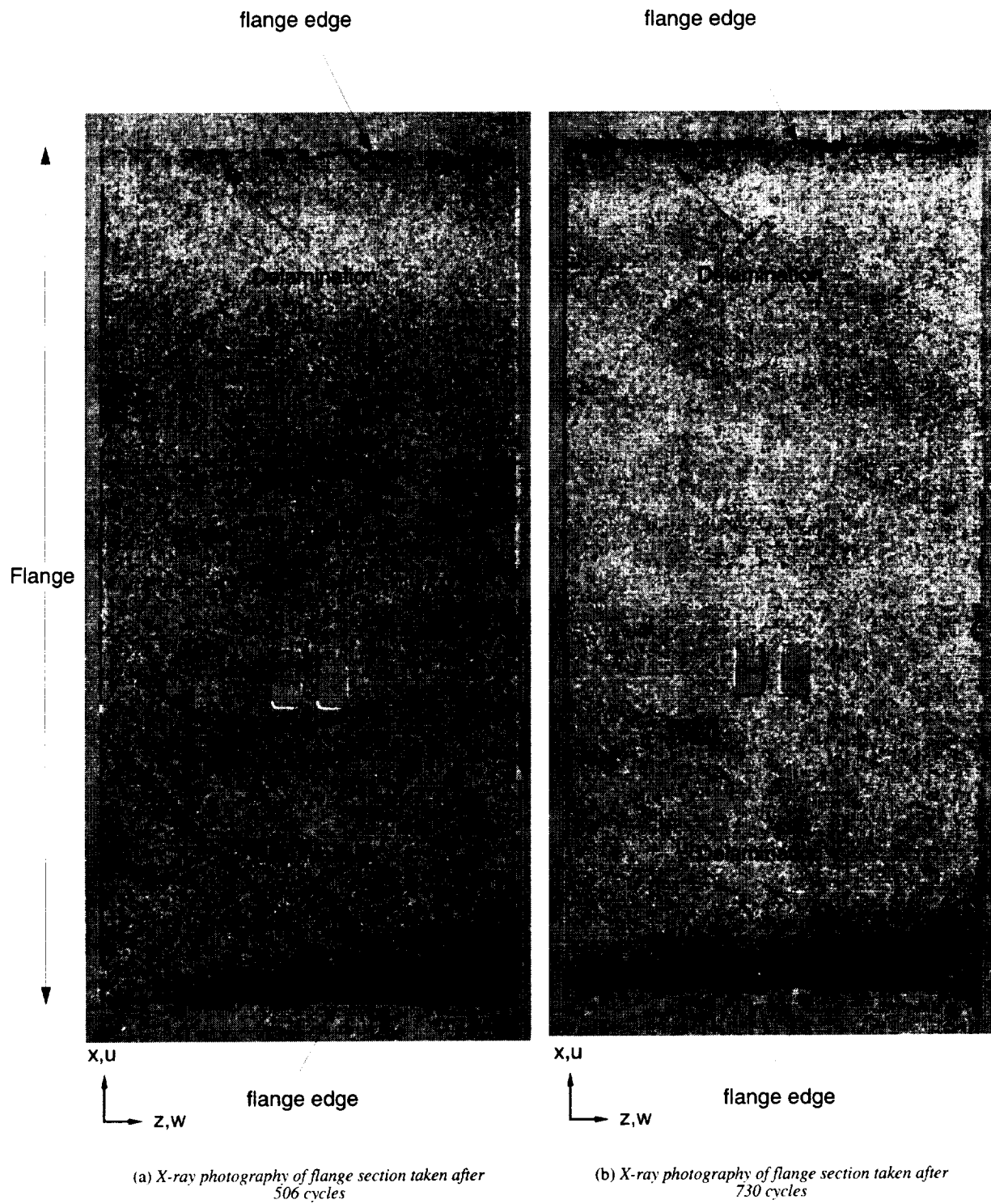
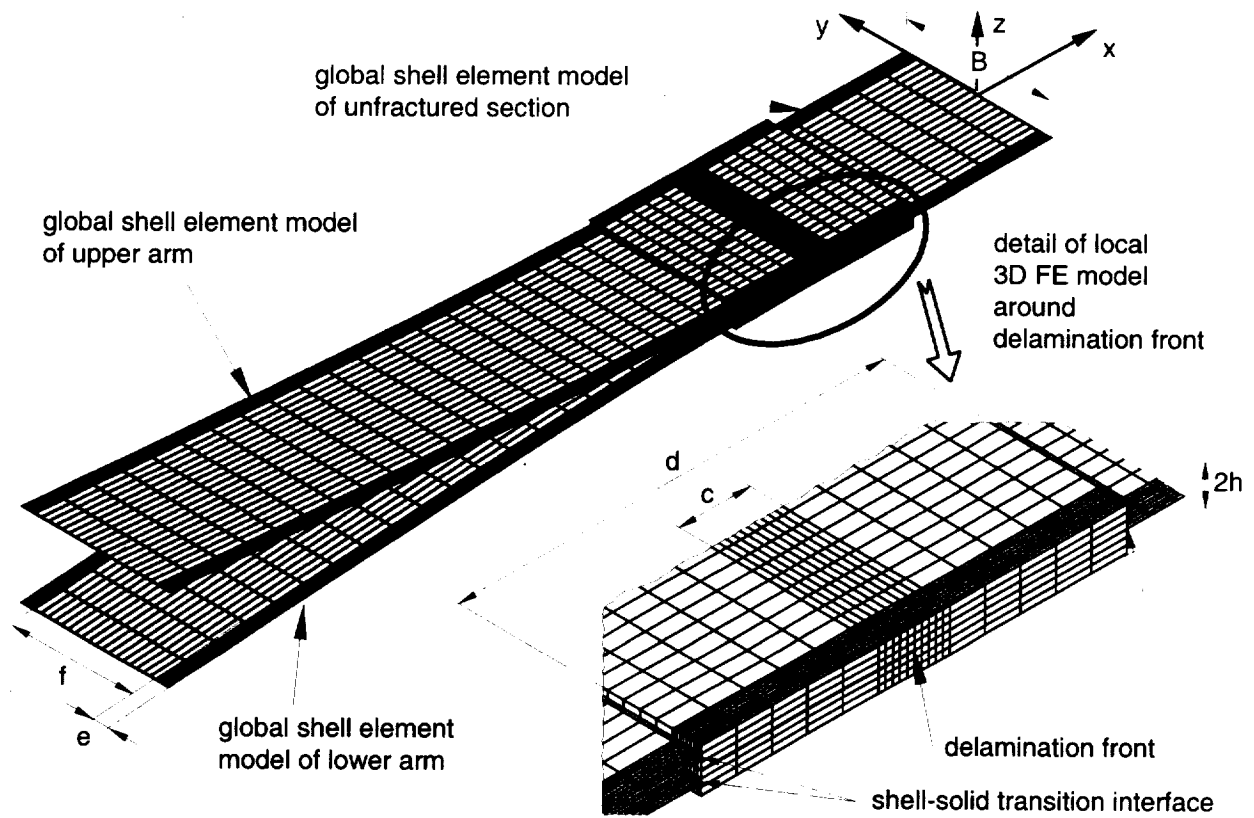
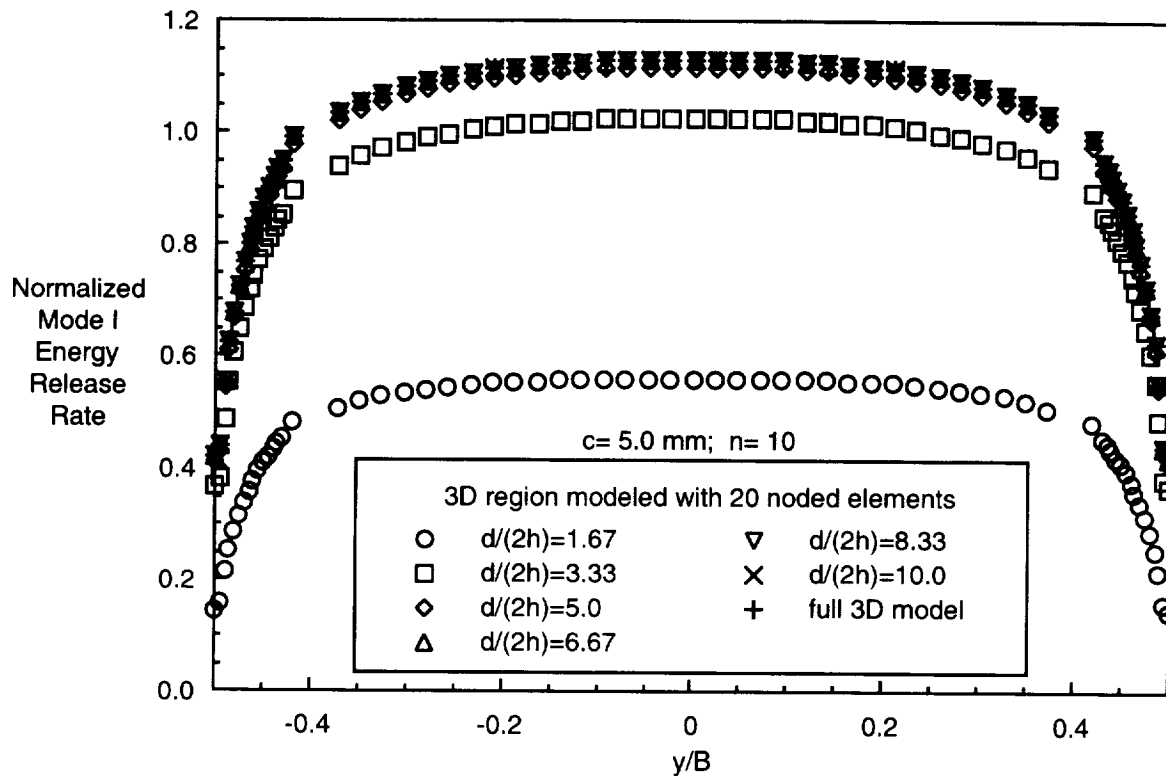


FIGURE 12. Damage progression in skin/stringer debond specimen

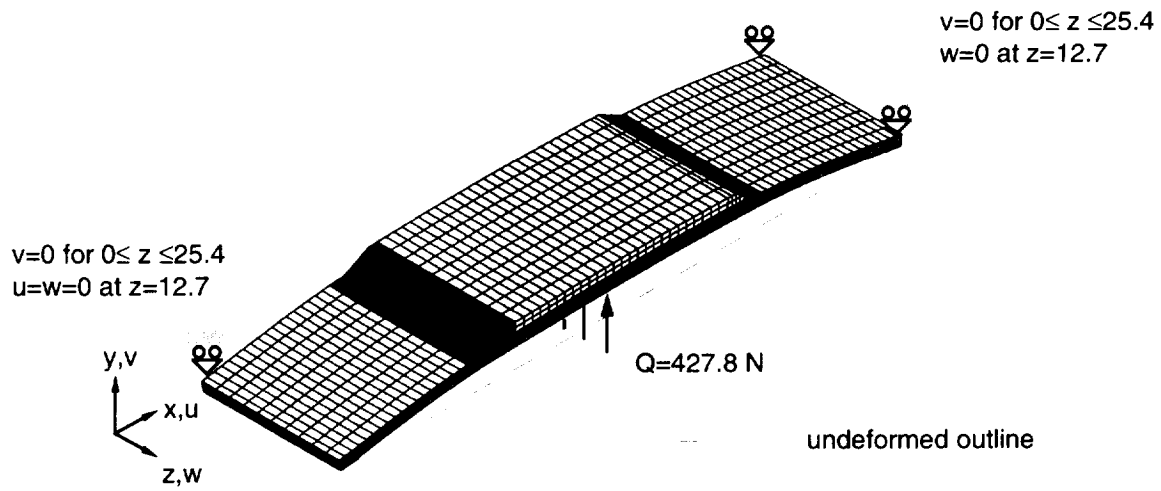


(a) FE model and detail around delamination front
($c = 5 \text{ mm}$, $d = 30 \text{ mm}$, $e = 2 \text{ mm}$, $f = 21.0 \text{ mm}$, $2h = 3.0 \text{ mm}$, $B = 25.0 \text{ mm}$)

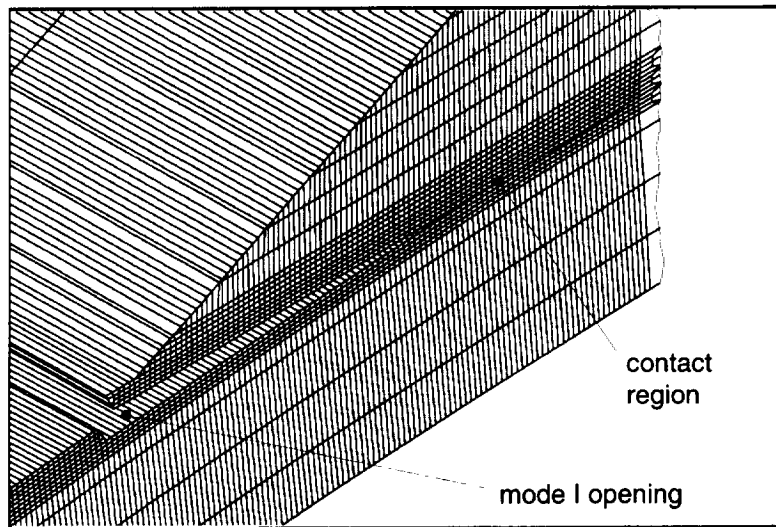


(b) Strain energy release rate distribution across the width

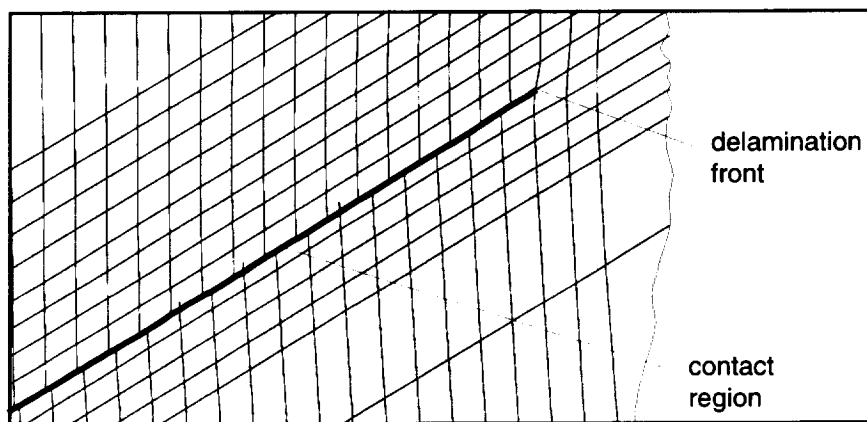
FIGURE 13. Shell/3D Finite element model of a DCB Specimen with $[0]_{24}$ layup.



(a) Deformed three-dimensional model with load and boundary conditions



(b) Detail of deformed model of damaged specimen

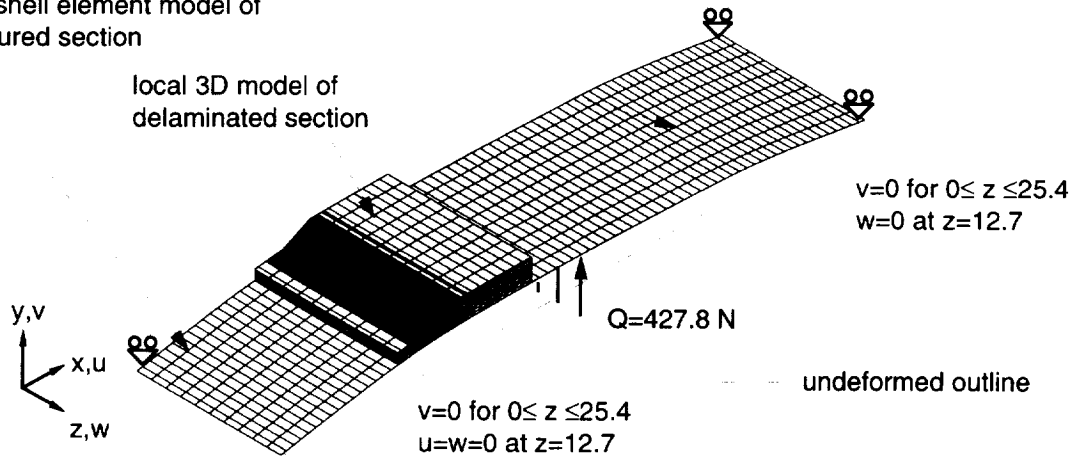


(c) Detail of contact region

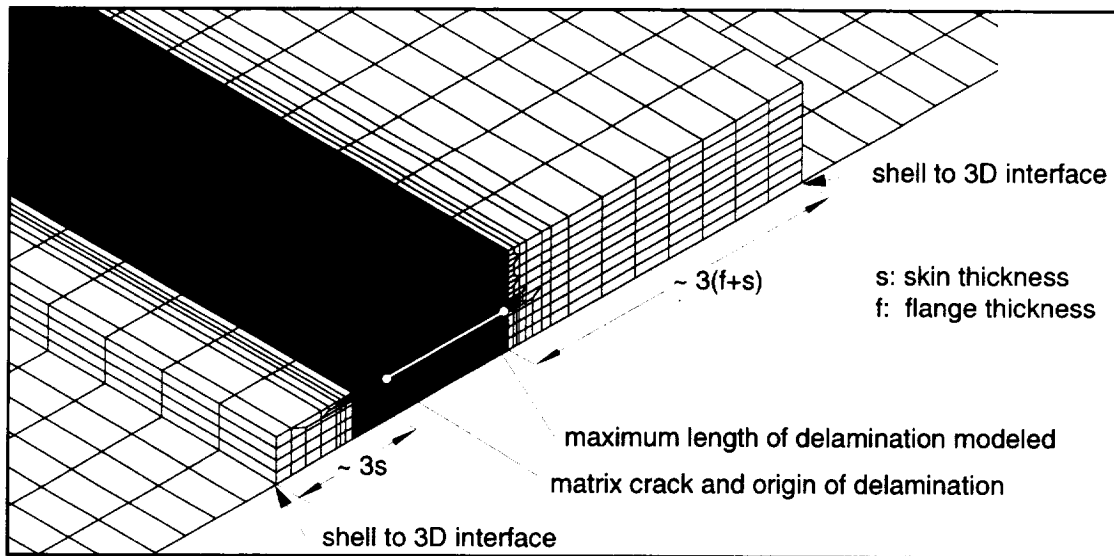
FIGURE 14. Full three-dimensional model of skin/flange specimen subjected to three-point bending

global shell element model of
unfractured section

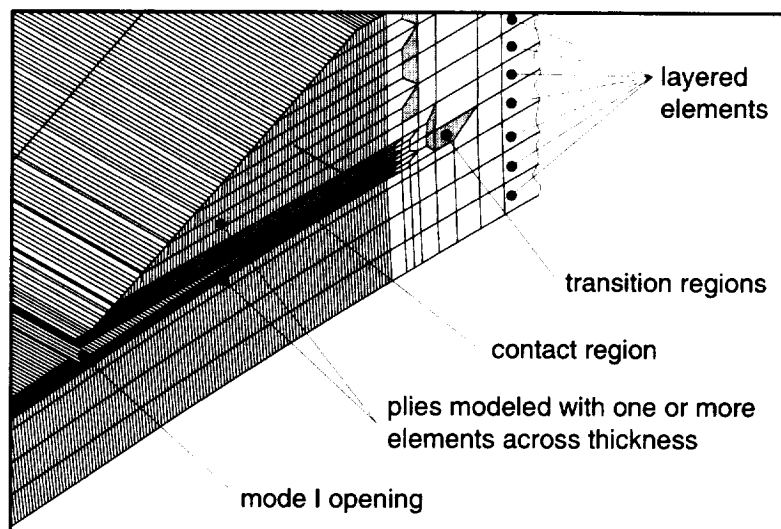
local 3D model of
delaminated section



(a) Deformed shell/3D model with load and boundary conditions



(b) Detail of undeformed local 3D model and shell to 3D interface region



(c) Detail of deformed model of damaged specimen

FIGURE 15. Shell/3D model of skin/flange specimen subjected to three-point bending

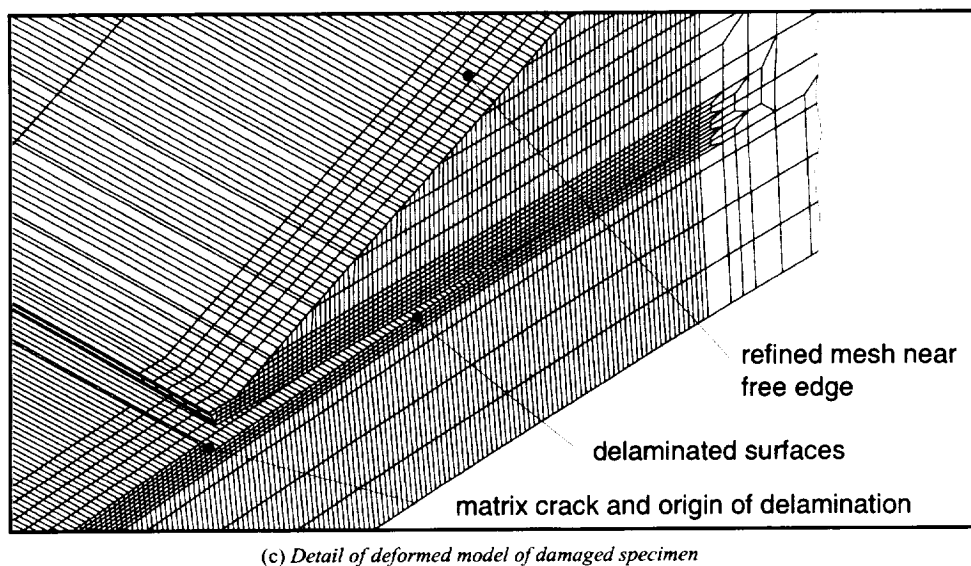
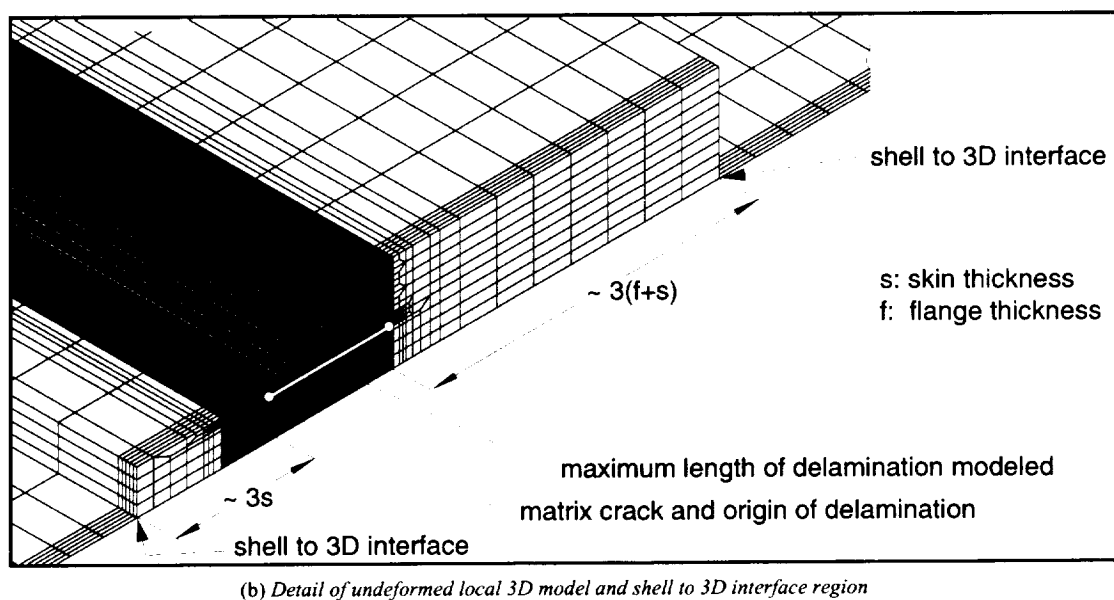
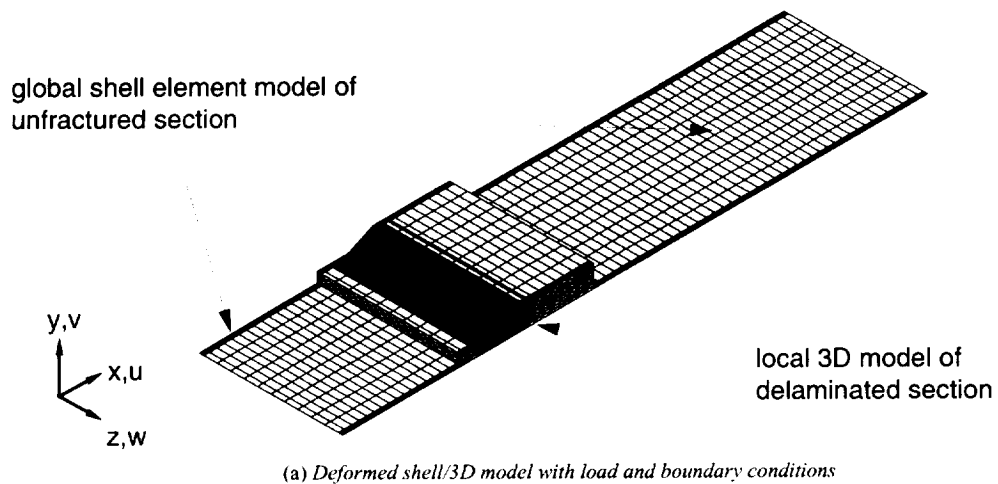


FIGURE 16. Shell/3D model of skin/flange specimen with fine mesh near the edge

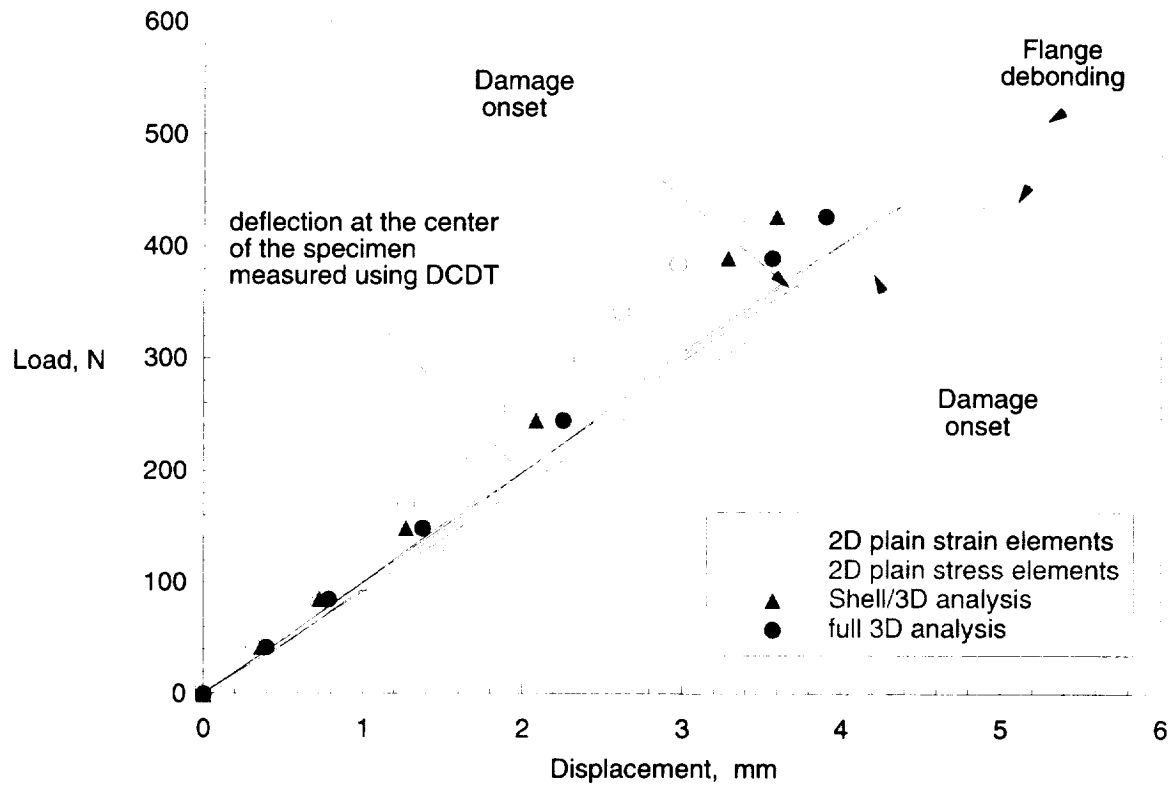


FIGURE 17. Load-displacement plots for three-point bending tests

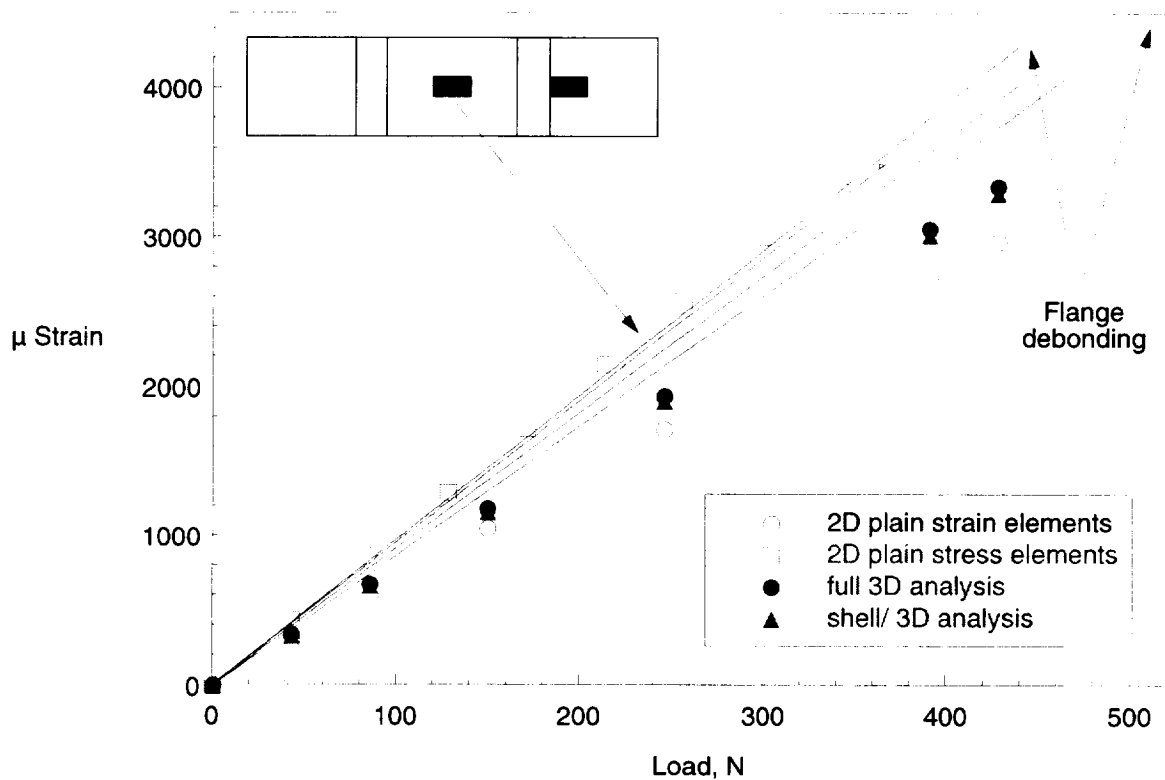


FIGURE 18. Flange strain-load plots for three-point bending tests

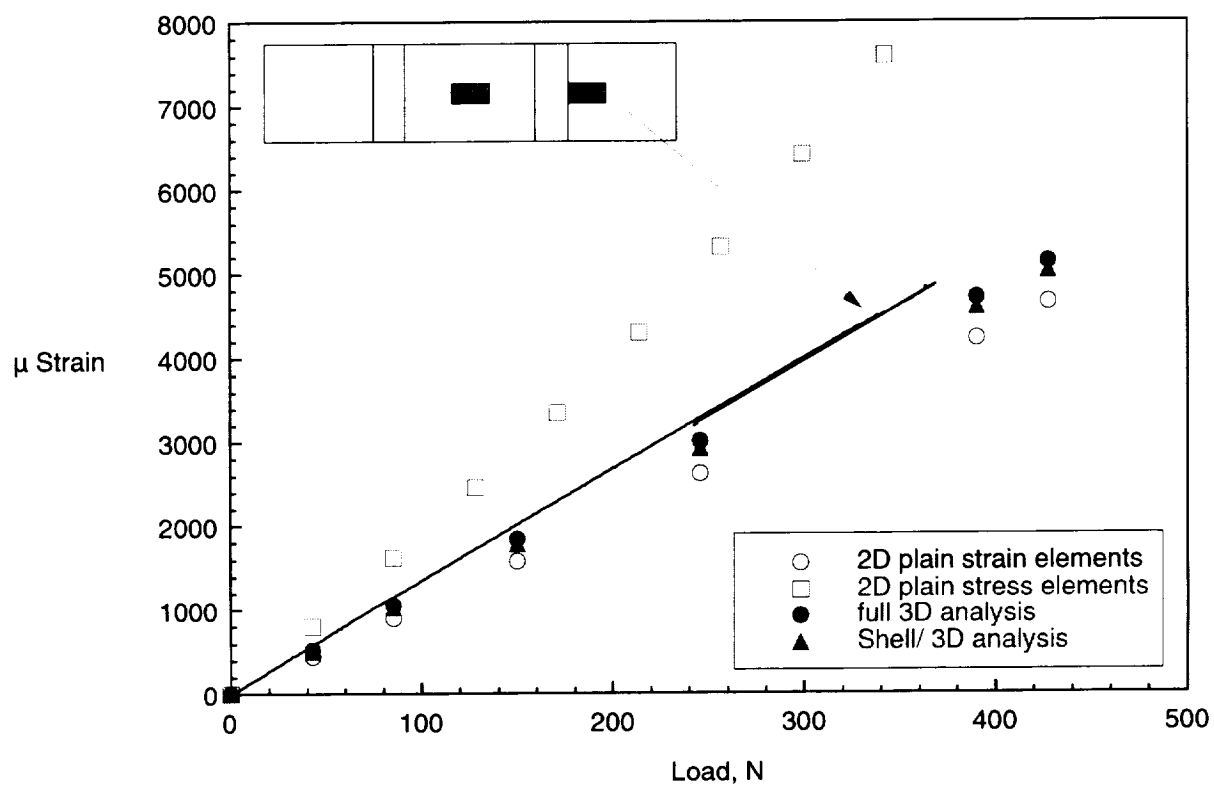


FIGURE 19. Skin strain-load plot for three-point bending tests.

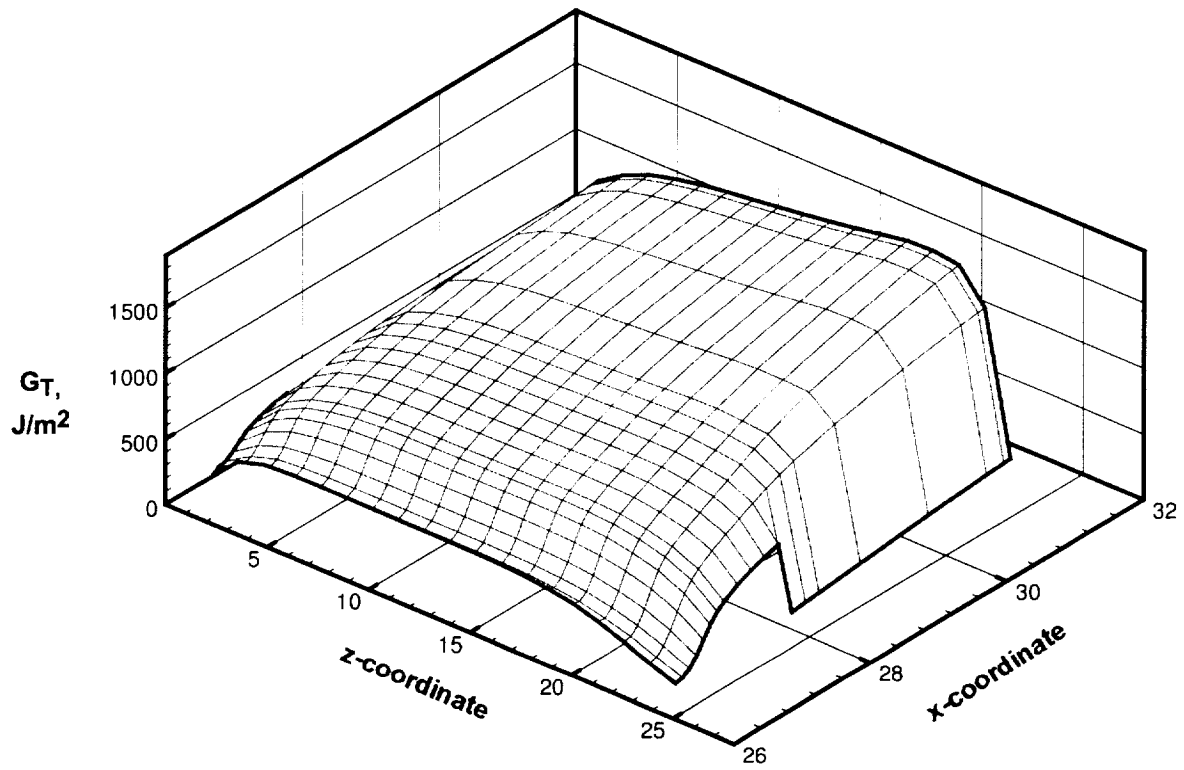


FIGURE 20. Computed total energy release rate distribution for three-point bending test.

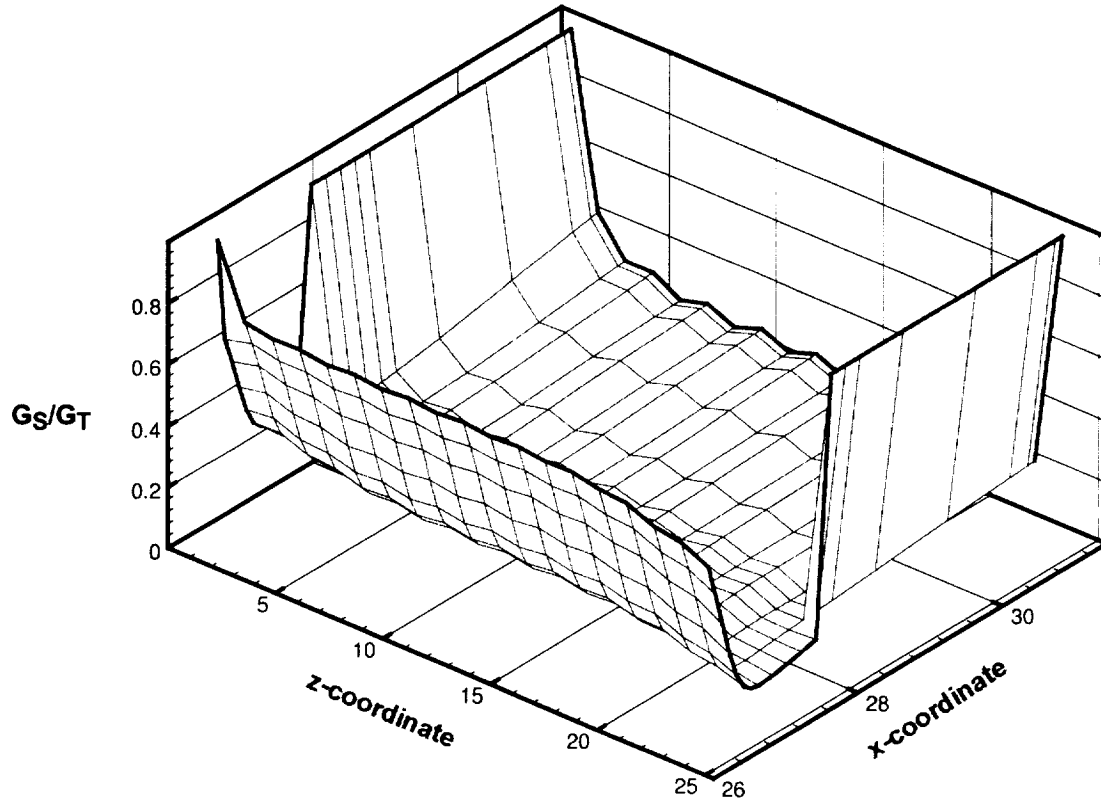


FIGURE 21. Computed mixed mode ratio G_S/G_T for three-point bending test.

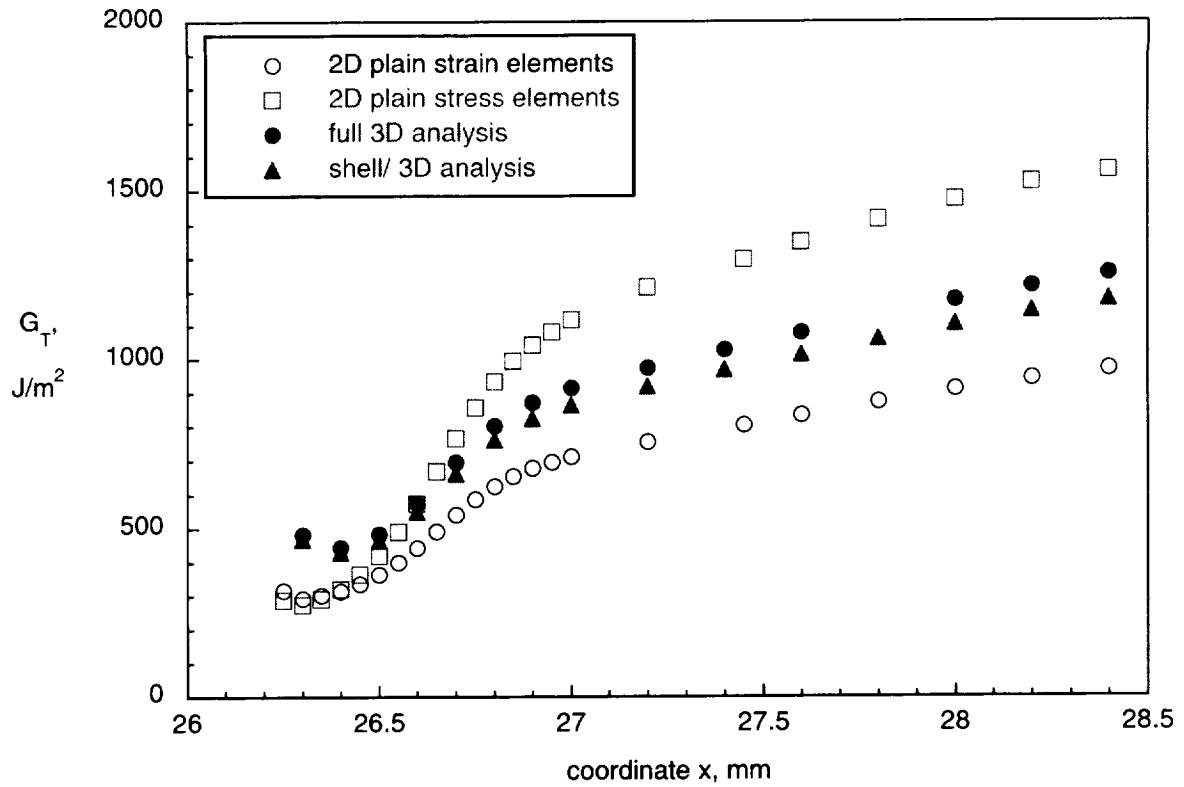


FIGURE 22. Computed total strain energy release rate at center of specimen width ($z = 12.7$ mm) for three-point bending test

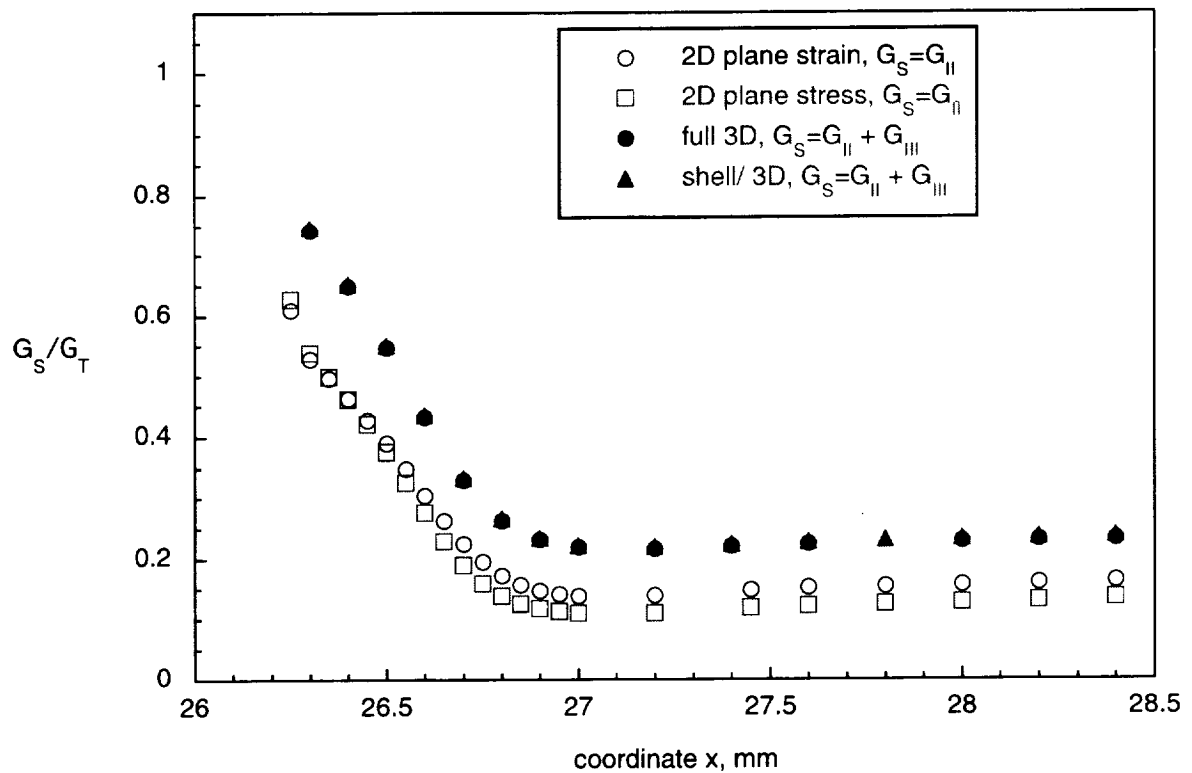


FIGURE 23. Computed mixed mode ratio at center of specimen width ($z = 12.7$ mm) for three-point bending test

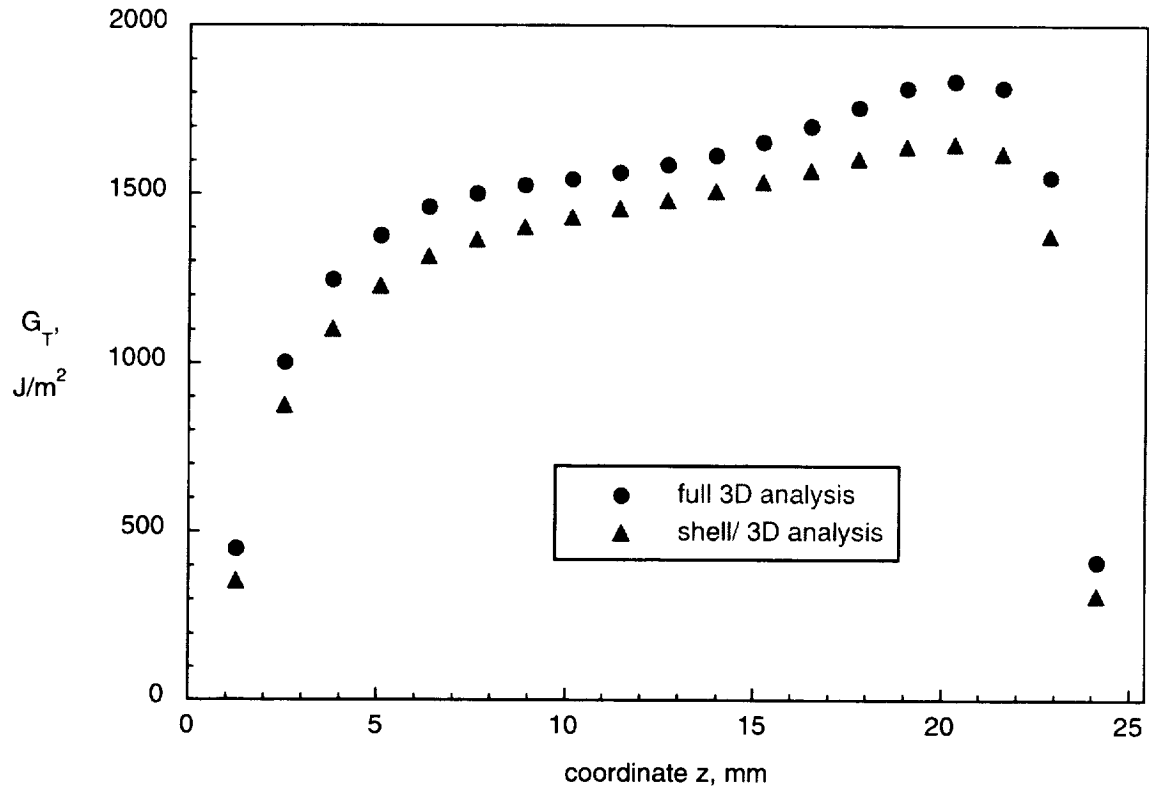


FIGURE 24. Computed total energy release rate across the width of the specimen at $x = 31.2$ mm for three-point bending test

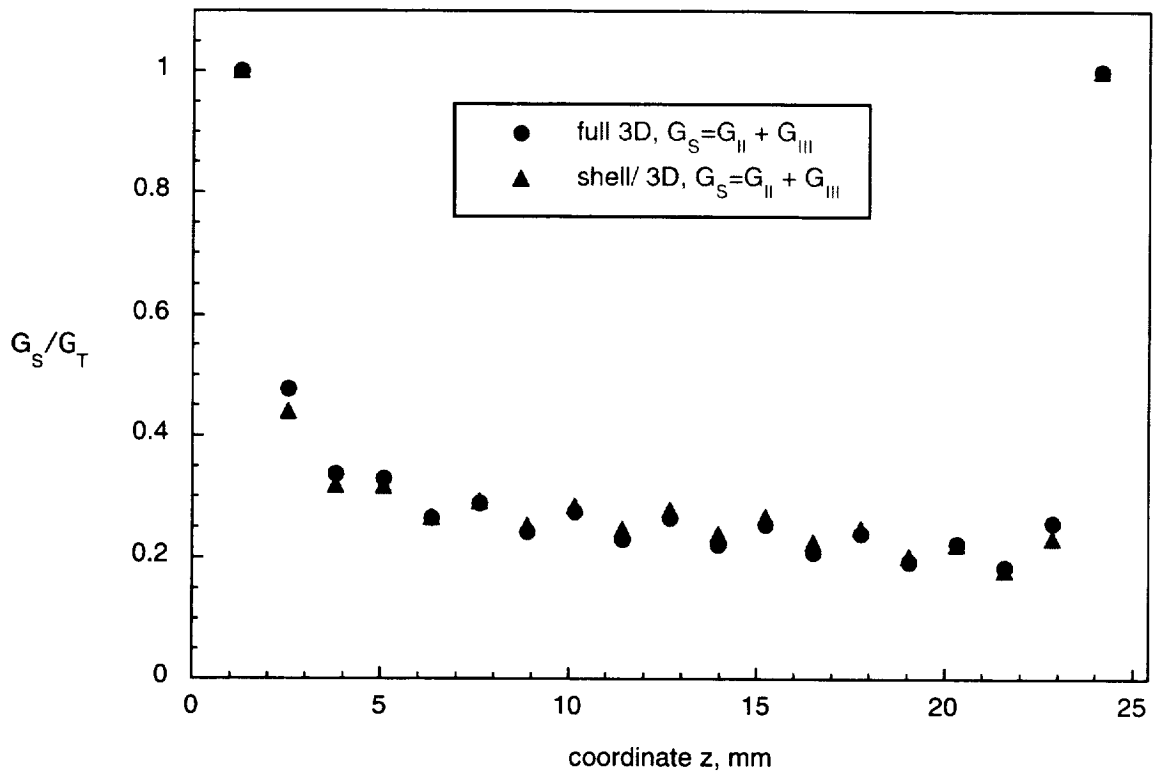


FIGURE 25. Computed mixed mode ratio across the width of the specimen at $x = 31.2$ mm for three-point bending test

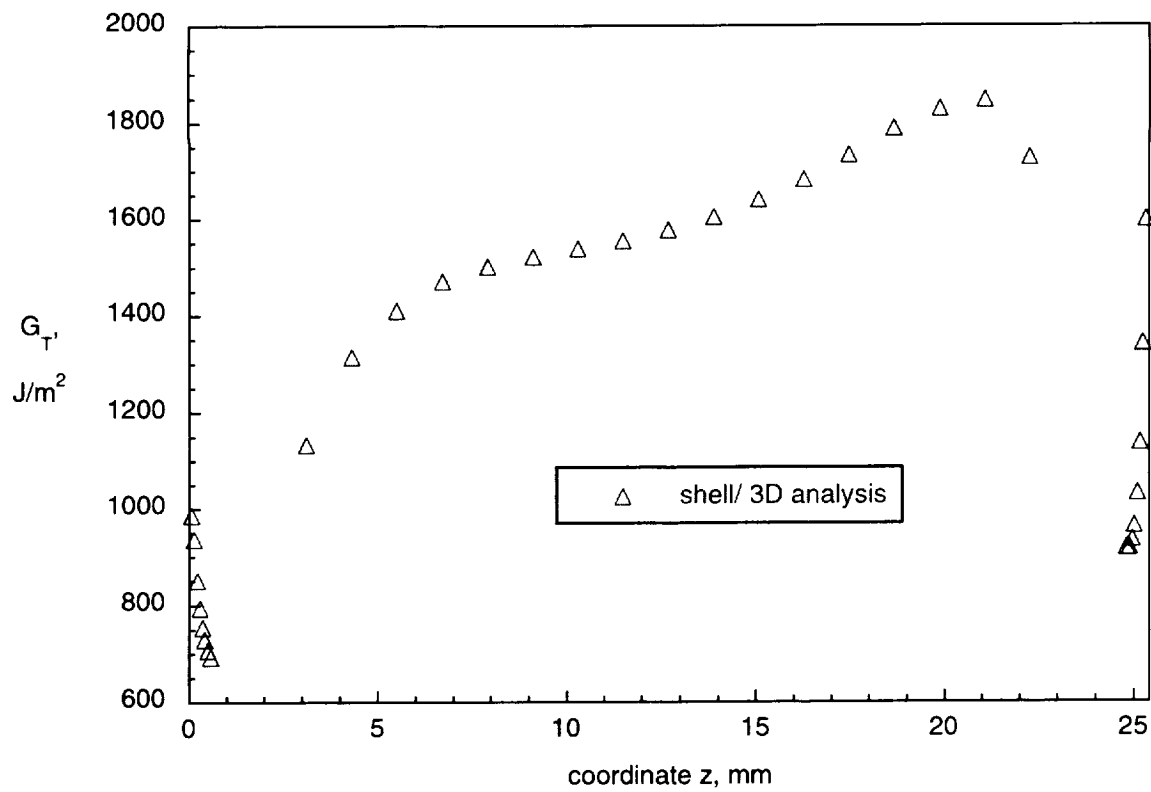


FIGURE 26. Computed total energy release rate across the width of the specimen at $x = 31.2$ mm for three-point bending test

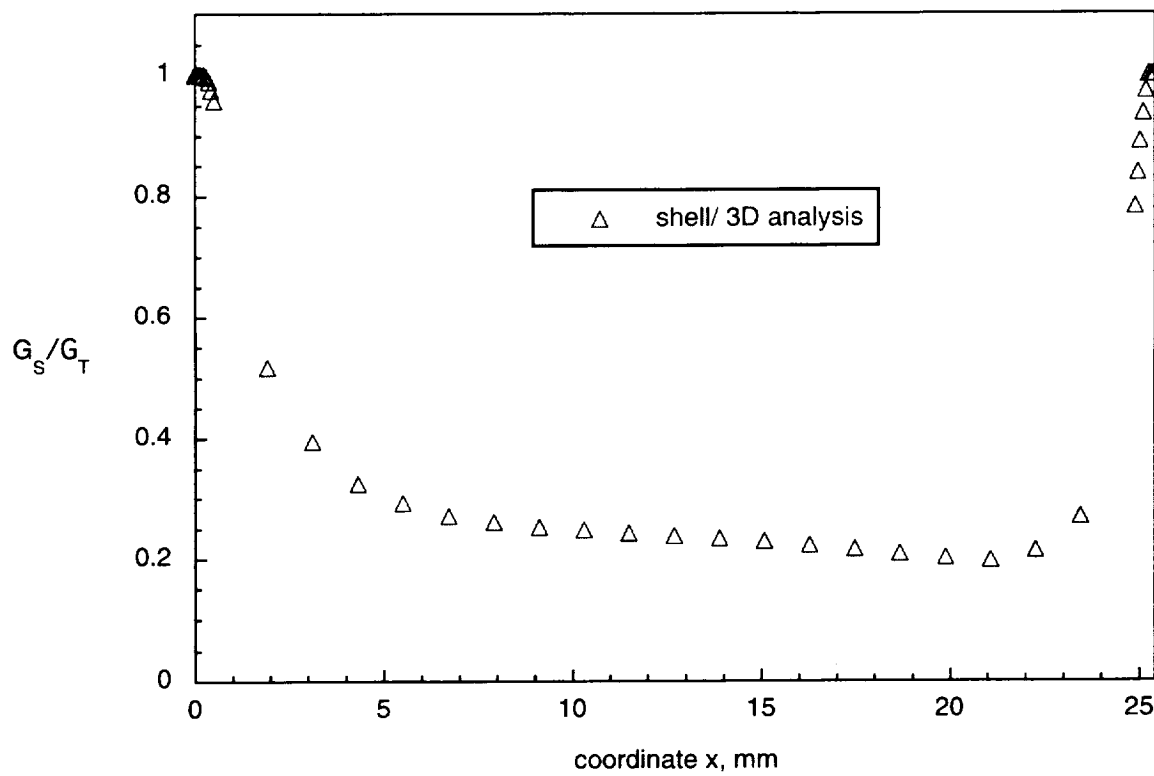


FIGURE 27. Computed mixed mode ratio across the width of the specimen at $x = 31.2$ mm for three-point bending test

REPORT DOCUMENTATION PAGE			Form Approved OMB No. 0704-0188	
Public reporting burden for this collection of information is estimated to average 1 hour per response, including the time for reviewing instructions, searching existing data sources, gathering and maintaining the data needed, and completing and reviewing the collection of information. Send comments regarding this burden estimate or any other aspect of this collection of information, including suggestions for reducing this burden, to Washington Headquarters Services, Directorate for Information Operations and Reports, 1215 Jefferson Davis Highway, Suite 1204, Arlington, VA 22202-4302, and to the Office of Management and Budget, Paperwork Reduction Project (0704-0188), Washington, DC 20503.				
1. AGENCY USE ONLY (Leave blank)	2. REPORT DATE October 2002	3. REPORT TYPE AND DATES COVERED Contractor Report		
4. TITLE AND SUBTITLE ANALYSIS OF COMPOSITE SKIN-STIFFENER DEBOND SPECIMENS USING VOLUME ELEMENTS AND A SHELL/3D MODELING TECHNIQUE		5. FUNDING NUMBERS C NAS1-97046 WU 505-90-52-01		
6. AUTHOR(S) Ronald Krueger and Pierre J. Minguet				
7. PERFORMING ORGANIZATION NAME(S) AND ADDRESS(ES) ICASE Mail Stop 132C NASA Langley Research Center Hampton, VA 23681-2199		8. PERFORMING ORGANIZATION REPORT NUMBER ICASE Report No. 2002-38		
9. SPONSORING/MONITORING AGENCY NAME(S) AND ADDRESS(ES) National Aeronautics and Space Administration Langley Research Center Hampton, VA 23681-2199		10. SPONSORING/MONITORING AGENCY REPORT NUMBER NASA/CR-2002-211947 ICASE Report No. 2002-38		
11. SUPPLEMENTARY NOTES Langley Technical Monitor: Dennis M. Bushnell Final Report Submitted to the American Society of Composites (ASC).				
12a. DISTRIBUTION/AVAILABILITY STATEMENT Unclassified Unlimited Subject Category 34 Distribution: Nonstandard Availability: NASA-CASI (301) 621-0390		12b. DISTRIBUTION CODE		
13. ABSTRACT (Maximum 200 words) The debonding of a skin/stringer specimen subjected to tension was studied using three-dimensional volume element modeling and computational fracture mechanics. Mixed mode strain energy release rates were calculated from finite element results using the virtual crack closure technique. The simulations revealed an increase in total energy release rate in the immediate vicinity of the free edges of the specimen. Correlation of the computed mixed-mode strain energy release rates along the delamination front contour with a two-dimensional mixed-mode interlaminar fracture criterion suggested that in spite of peak total energy release rates at the free edge the delamination would not advance at the edges first. The qualitative prediction of the shape of the delamination front was confirmed by X-ray photographs of a specimen taken during testing. The good correlation between prediction based on analysis and experiment demonstrated the efficiency of a mixed-mode failure analysis for the investigation of skin/stiffener separation due to delamination in the adherents. The application of a shell/3D modeling technique for the simulation of skin/stringer debond in a specimen subjected to three-point bending is also demonstrated. The global structure was modeled with shell elements. A local three-dimensional model, extending to about three specimen thicknesses on either side of the delamination front was used to capture the details of the damaged section. Computed total strain energy release rates and mixed-mode ratios obtained from shell/3D simulations were in good agreement with results obtained from full solid models. The good correlations of the results demonstrated the effectiveness of the shell/3D modeling technique for the investigation of skin/stiffener separation due to delamination in the adherents.				
14. SUBJECT TERMS composite materials, delamination, finite element analysis, fracture mechanics		15. NUMBER OF PAGES 38		
		16. PRICE CODE A03		
17. SECURITY CLASSIFICATION OF REPORT Unclassified	18. SECURITY CLASSIFICATION OF THIS PAGE Unclassified	19. SECURITY CLASSIFICATION OF ABSTRACT	20. LIMITATION OF ABSTRACT	